Direct Measurement of the pp Solar Neutrino Interaction Rate in Borexino

DIRECT MEASUREMENT OF THE *PP* SOLAR NEUTRINO INTERACTION RATE IN BOREXINO

A Dissertation Presented

by

KEITH OTIS

Submitted to the Graduate School of the
University of Massachusetts Amherst in partial fulfillment
of the requirements for the degree of

DOCTOR OF PHILOSOPHY

May 2014

Physics

DIRECT MEASUREMENT OF THE *PP* SOLAR NEUTRINO INTERACTION RATE IN BOREXINO

A Dissertation Presented

by

KEITH OTIS

Approved as to style and content by:

Andrea Pocar, Chair

Laura Cadonati, Member

Krishna Kumar, Member

Grant Wilson, Member

Rory Miskimen, Department Chair
Physics

To my family; you have each helped me become who I am today.

FOREWORD

The results of this dissertaion are self contained and all the information needed to reach its conclustions has been presented in detail. However, I have made an effort to keep this work directed towards its goal of presenting the results of the first direct measurement of *pp* solar neutrinos and as a result much of the work done in the millions of man-hours put into Borexino has been reduced to a sentence and single citation to the relevant publication, thesis, conference presentation, or internal document. This was done not to minimize the extreme amount of work that was done by others to make this dissertation a success but to provide a detailed, yet concise, roadmap for the reader in understanding the detector and methods that led to this result as well as its impact on our understanding of the world around us.

ABSTRACT

DIRECT MEASUREMENT OF THE *PP* SOLAR NEUTRINO INTERACTION RATE IN BOREXINO

MAY 2014

KEITH OTIS

B.Sc., UNIVERSITY OF MASSACHUSETTS AMHERST

M.A., BOSTON UNIVERSITY

Ph.D., UNIVERSITY OF MASSACHUSETTS AMHERST

Directed by: Professor Andrea Pocar

This dissertation presents the first direct detection of *pp* solar neutrinos within Borexino, the underground liquid-scintilator detector located at the Gran Sasso National Labratory(LNGS) in Italy, designed to measure the interaction of neutrinos through neutrino-electron elastic scattering. The rate of scattering in Borexino from the *pp* solar neutrino spectrum is measured to be $155 \pm 16(stat) \pm 13(sys)$ counts per day per 100 tonnes. With this measurement we are able to rule out the no oscillation hypothesis at the 2σ C.L. and the results agree with Standard Solar Model predictions within 1.1σ. These neutrinos are from the keystone proton-proton fusion reaction in the Sun and collectively they vastly outnumber those from the reactions that follow. Their detection is an important step towards completing solar neutrino spectroscopy and verifies our understanding of the Sun.

TABLE OF CONTENTS

LIST OF TABLES

Table **Page**

LIST OF FIGURES

Figure **Page**

INTRODUCTION

Neutrinos (ν) are particles that are produced in processes that involve radioactive decays or the nuclear fusion that powers stars. They have been detected from nuclear reactors, the decay of heavy elements inside the Earth, the interaction of cosmic rays with Earth's atmosphere, the fusion of elements in stars, and a supernova from the spectacular collapse of a massive star in a near by galaxy.

The strongest source near Earth of these neutral particles with extremely low mass is the Sun. Neutrinos are produced in the core Sun via a series of nuclear reactions. The predominant process is the proton-proton (pp) fusion chain which is also the primary source of solar energy. In this chain, electron neutrinos (ν_e) are produced in a number of the reactions with each one having a characteristic energy spectrum and flux. The number of neutrinos produced in the Sun is very large, resulting in a flux of solar neutrinos on Earth that is about 6 x $10^{10} cm^{-2} s^{-1}$.

Neutrinos interact only weakly with matter. They are extremely difficult to detect and this, in turn, drives the development of very sensitive detectors and novel construction and analysis techniques to measure them. This same property allows them to escape the core of the Sun, where they are produced, without being affected by the dense matter in the regions of their production. Due to this we are able to use nuetrinos to study the inner processes of the Sun.

Solar neutrino experiments have been used since their advent in the 1970s as sensitive tools to test both particle physics and astrophysical models. They were first constructed to test the hypothesis that the Sun is primarily powered by nuclear fusion reactions. Through early 2014, the neutrinos from the primary reaction in the base of the pp chain have not been directly detected. Despite being the most abundant of the solar neutrino species the low energy of these neutrinos has placed them below the threshold of previous detectors that have searched for the individual neutrino species. A successful detection of these neutrinos is a remarkable accomplishment in ulta-low background detector development and neutrino measurements. It provides important confirmation of current astrophysical models as well as a check that the internal workings of the Sun have not changed significantly in the last million years (photons produced in the core of the Sun take $\sim 10^6$ years to reach Earth whereas neutrinos take ~ 10 minutes).

CHAPTER 1

SOLAR NEUTRINO PHYSICS

Neutrinos were first directly detected by Cowan and Reines in 1953 [8] after being proposed theoretically by Wolfgang Pauli in 1930 as an explanation for the observed lack of energy and spin conservation in β decays [9]. In the years since, neutrinos have been the subject of many experiments and theoretical studies, with far reaching influence on the fields of particle physics, astrophysics, cosmology and geophysics. This chapter begins by presenting some of the basic properties of neutrinos and then follows with a discussion on solar neutrinos.

1.1 Neutrinos and the Standard Model

The 1970s, with the discovery of neutral current interactions and the formulation of the *Standard Model*(SM), was when neutrinos began to be fully understood in the context of the rest of our knowledge of physics at the time. Neutrinos are leptons with a very low mass (they are massless in the SM) and are the only chargeless, spin-1/2 particles. They interact only via the weak nuclear force which makes neutrinos difficult to detect. There are three distinct neutrino flavors that are the eigenstates of the weak interaction: the electron neutrino (ν_e), muon neutrino (ν_μ), and tau neutrino (ν_τ), each named for the charged lepton that they interact with. The eigenstates of the weak interaction do not coincide with the mass eigenstates of the neutrino(ν_1, ν_2, and ν_3). It's this property of neutrinos that causes them to oscillate between weak states as they propagate [1]. The total number of light neutrino species is restricted by the invisible width of the Z^0 boson, measured in electron-positron

Parameter	Value
Luminosity ($L_\odot$)	$3.8418 \times 10^{26} W$
	$2.3977 \times 10^{39} MeV/sec$
Radius ($R_\odot$)	$6.9598 \times 10^{10} cm$
Mass ($M_\odot$)	$1.9884 \times 10^{33} g$
Core temperature	$\sim 1.55 \times 10^{7} K$
	$\sim 1.34 keV$
Core density	$\sim 153 g/cm^3$
Surface, heavy element to hydrogen ratio (Z/X)	0.0229 (GS98)
	0.0178 (AGSS09)
Mean distance to Earth (AU)	$1.49598 \times 10^{13} cm$
Solar constant ($K_\odot = L_\odot/4\pi(AU)^2$)	$8.5339 \times 10^{11} MeV/cm^2/sec$

Table 1.1. The main solar parameters for the Standard Solar Model(SSM)

collisions, at 2.9840 ± 0.0082 [1]. The best limits on the total number of neutrino species comes from cosmological measurements and has been found to be 3.30 ± 0.27 [10].

1.2 Neutrino Production in the Sun and the Standard Solar Model

The discovery of relativity in the 1900s provided a relationship between mass and energy. This paved the way for the proposal of the first mechanism that could explain the measured energy output of the Sun over the geologic time scales of billions of years known to have elapsed. The solution to this was a system that allowed the main component of the Sun, hydrogen, to be converted in a helium-nucleus and 26.7 MeV of energy.

The collective process of converting hydrogen into helium is summarized by:

$$4p \rightarrow^4 He + 2e^+ + 2\nu_e. \tag{1.1}$$

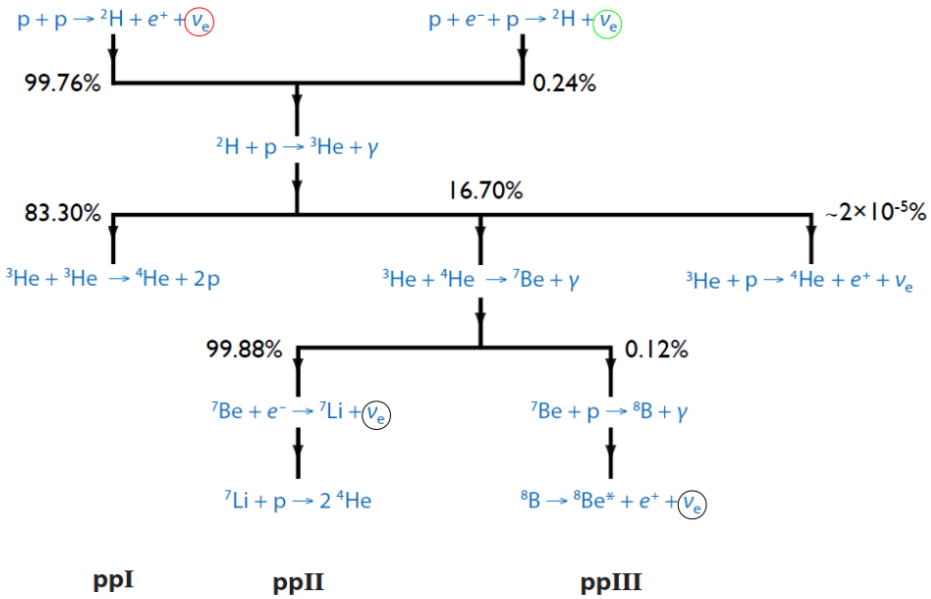

Figure 1.1. Shown above are the three predominant *pp* chain branches, each of which is labeled by its identifying neutrino. The *pp* neutrino is circled in red and is the dominant source of the deuterium used in the *pp* chain. The *pep* neutrino, circled in green, comes from the other reaction that can produce deuterium for the *pp* chain. Figure adapted from [5] A small fraction of the Sun's energy also comes from a secondary process called the CNO cycle. The spectra of these neutrinos can be seen in Figure 1.2 in addition to those from the *pp* cycle.

This process was first described in detail by Hans Bethe in 1939 [11] and the subject was developed in detail by John N. Bahcall who then reviewed it in his book [12] and later on his website (http://www.sns.ias.edu/ jnb/).

In stars of mass similar to that of the Sun, the predominant process that converts hydrogen into helium is known as the proton-proton (*pp*) chain (see Figure 1.1). In more massive stars processes with heavier elements come into play in the fusion reactions [12]. The *pp* chain has five branches that each produce a distinct neutrino; the spectra for these neutrinos is shown in Figure 1.2

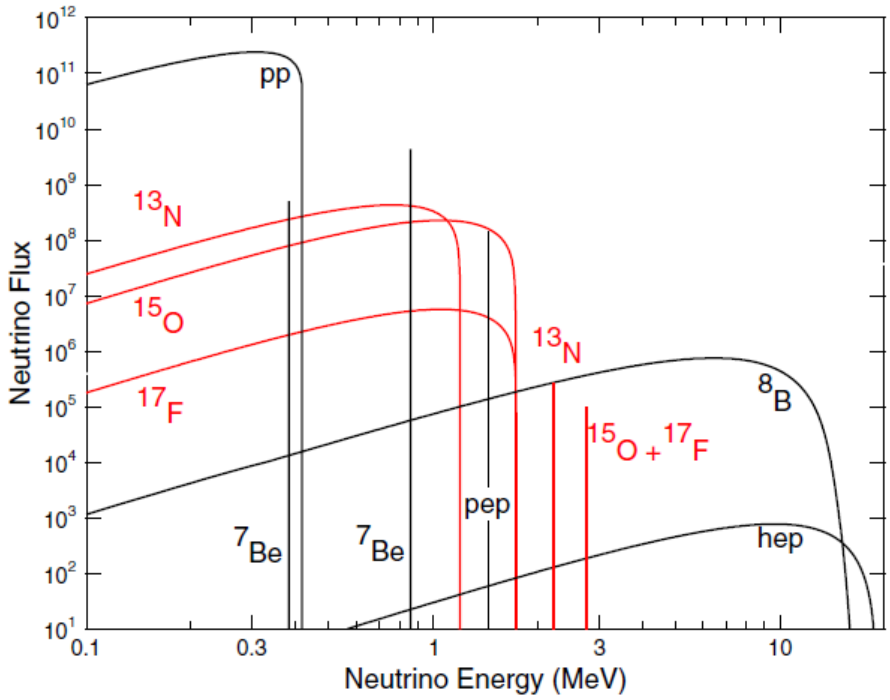

Figure 1.2. Shown in black are the spectra for the neutrinos in the *pp* chain. In red are those produced by the CNO cycle (^{13}N, ^{15}O, and ^{17}F). Mono-energetic, line fluxes are in units of cm^{-2}sec^{-1} and continuous spectra are in units of cm^{-2}sec^{-1}MeV^{-1}. This figure is in log-scale and it can be seen that the *pp* neutrinos make up nearly all the Solar neutrino flux. (Adapted from [5])

Solar models describe the ways that the four fundamental interactions determine the structure and evolution of our Sun based on the results of experiments and predictions from many different areas of physics. These models are characterized by the values of several paramters. The current best estimate of these parameters are enumerated in Table 1.1. The Standard Solar Model makes very precise predictions about the neutrino flux on Earth. Using the expression derived in [13] in combination with the production rates predicted by the Standard Solar Model, we are able to calculate the estimated flux on Earth for the neutrinos from the different solar processes. These estimates can be found in Table 1.3. Below we make a simple, model-independent estimate of this flux from basic principles and some reasonable assumptions.

From Eq. 1.1 we know that two neutrinos are generated for every 26.7 MeV of energy produced in the Sun. Ignoring the energy that the neutrinos themselves carry away, we come to the following simple relation for the expected neutrino flux at Earth:

$$\phi \geq 2 \times \frac{K_{\odot}}{Q} \geq 6.4 \times 10^{10} cm^{-2} sec^{-1} \tag{1.2}$$

where $K_{\odot}$ is the average solar constant (see Table 1.1) and Q = 26.7 MeV.

If we assume that the fusion reactions described previously in this chapter are the correct source of power for the Sun we can then sum over the resulting neutrino spectra to arrive at a precise equality between their flux and the solar luminosity. This equation is referred to as the luminosity constraint [14]

$$\frac{L_{\odot}}{4\pi(AU)^2} = \sum_i \alpha_i \phi_i, \tag{1.3}$$

where $L_{\odot}$ is the solar luminosity at Earth's surface and 1 AU is the average Sun-Earth distance and the sum is over the individual neutrino species.

There are several subsets of what we call the Standard Solar Model. Each of these cases specifies a value for all of the important parameters and this in turn allows for

a calculation of the production rate and spectra of all of the neutrinos from each of the processes in the Sun [1] (See Table 1.3 and Figure 1.2).

1.3 Neutrino Oscillation

All of the neutrinos produced in the Sun are electron neutrinos because the energy of the processes is far below that of the muon and the tau. The fact that the weak ($\alpha = e, \mu, \tau$) and mass (i = 1,2,3) eigenstates of the neutrino do not coincide leads to a process of mixing. Transformations between the eigenstates are described by the unitary Pontecorvo-Maki-Nakagawa-Sakata (PMSN) mixing matrix U:

$$|\nu_\alpha\rangle = \sum_i U_{\alpha i}|\nu_i\rangle \Leftrightarrow |\nu_i\rangle = \sum_\alpha U^\dagger_{\alpha i}|\nu_\alpha\rangle \tag{1.4}$$

where

$$U = \begin{bmatrix} U_{e1} & U_{e2} & U_{e3} \\ U_{\mu 1} & U_{\mu 2} & U_{\mu 3} \\ U_{\tau 1} & U_{\tau 2} & U_{\tau 3} \end{bmatrix}. \tag{1.5}$$

Let us consider a neutrino produced in the Sun at a position, $\vec{x} = 0$ and time, $t = 0$. This neutrino will be in a week eigenstate $|\nu_e\rangle$. If we allow this neutrino to be of any flavor eigenstate we have $|\nu_\alpha\rangle$ and:

$$|\nu\rangle(\vec{x} = 0, t = 0) = |\nu_\alpha\rangle = \sum_i U_{\alpha i}|\nu_i\rangle. \tag{1.6}$$

This neutrino will propagate via its free Hamiltonian, the eigenstates of which are the mass eigenstates. Under the assumtion that only the center of the corresponding wave packet moves, we have a plane-wave solution for each neutrino eigenstate:

$$|\nu\rangle(\vec{x},t) = \sum_i U_{\alpha i} e^{-i(E_i t - \vec{p}_i \dot{\vec{x}})} |\nu_i\rangle \tag{1.7}$$

$$|\nu\rangle(\vec{x},t) = \sum_i U_{\alpha i} e^{-i(E_i t - p_i L)} |\nu_i\rangle \tag{1.8}$$

where E_i and $\vec{p}_i = p_i \hat{k}$ are the energy and momentum vectors of the appropriate mass eigenstate and $\vec{x} = L\hat{k}$ where $\hat{k}$ is the unit vector in the directon of the neutrino momentum.

When this neutrino reaches Earth and interacts with a detector the probability to observe it in the weak eigenstate $|\nu_\beta\rangle$ is:

$$P(\nu_\alpha \to \nu_\beta) = |\langle \nu_\beta | \nu \rangle(\vec{x},t)|^2 \tag{1.9}$$

$$= \left| \sum_i \sum_j \langle \nu_j | U^\dagger_{j\beta} U_{\alpha i} e^{-i(E_i t - p_i L)} | \nu_i \rangle \right|^2 \tag{1.10}$$

$$= \left| \sum_i U^*_{\beta i} U_{\alpha i} e^{-i(E_i t - p_i L)} \right|^2 \tag{1.11}$$

$$= \sum_i \sum_j U_{\alpha i} U^*_{\beta i} U^*_{\alpha j} U_{\beta j} e^{-i((E_i - E_j)t - (p_i - p_j)L)} \tag{1.12}$$

$$= \sum_i \sum_j |z_{\alpha\beta ij}| \, cos((E_i - E_j)t - (p_i - p_j)L - arg(z_{\alpha\beta ij})) \tag{1.13}$$

where $z_{\alpha\beta ij} \equiv U_{\alpha i} U^*_{\beta i} U^*_{\alpha j} U_{\beta j}$. In order to relate neutrino mass and oscillations we note that we can relate the distance travelled to the elapsed time and average wave packet velocity $\bar{v}$.

$$L \sim \bar{v} t \equiv \frac{p_i + p_j}{E_i + E_j} t \tag{1.14}$$

Using this we find that

$$(E_i - E_j)t - (p_i - p_j)L \sim \frac{m_i^2 - m_j^2}{p_i + p_j} L \equiv \frac{\Delta m_{ij}^2}{2\bar{p}} L \tag{1.15}$$

allowing us to write the transition probability as:

$$P(\nu_\alpha \to \nu_\beta) = \sum_i \sum_j |z_{\alpha\beta ij}| \, cos(\frac{\Delta m_{ij}^2}{2\bar{p}} L - arg(z_{\alpha\beta ij})). \tag{1.16}$$

This means that if there is an observation of a transition between different neutrino flavor states there must be a non-zero mass difference. This, in turn, implies that at least one of the neutrino masses is non-zero.

In the case of three neutrino flavors, the matrix describing vacuum oscillations can be parameterized by three mixing angles and six phases. If neutrinos are Dirac particles, where neutrinos and antineutrinos are different particles, then there exists only one physical phase, denoted at the CP-violating Dirac phase (δ). While Majorana neutrinos, where each neutrino is its own antiparticle, would have two additional phases (α_i). Factoring the general mixing matrix into these angles and phases we get:

$$U = \begin{bmatrix} c_{12}c_{13} & s_{12}c_{13} & s_{13}e^{-i\delta} \\ -s_{12}c_{23} - c_{12}s_{23}s_{13}e^{i\delta} & c_{12}c_{23} - s_{12}s_{23}s_{13}e^{i\delta} & s_{23}c_{13} \\ s_{12}s_{23} - c_{12}c_{23}s_{13}e^{i\delta} & -c_{12}s_{23} - s_{12}c_{23}s_{13}e^{i\delta} & c_{23}c_{13} \end{bmatrix} \begin{bmatrix} e^{i\alpha_1/2} & 0 & 0 \\ 0 & e^{i\alpha_2/2} & 0 \\ 0 & 0 & 1 \end{bmatrix} \tag{1.17}$$

$$= \begin{bmatrix} 1 & 0 & 0 \\ 0 & c_{23} & s_{23} \\ 0 & -s_{23} & c_{23} \end{bmatrix} \begin{bmatrix} c_{13} & 0 & s_{13}e^{-i\delta} \\ 0 & 1 & 0 \\ -s_{13}e^{i\delta} & 0 & c_{13} \end{bmatrix} \begin{bmatrix} c_{12} & s_{12} & 0 \\ -s_{12} & c_{12} & 0 \\ 0 & 0 & 1 \end{bmatrix} \begin{bmatrix} e^{i\alpha_1/2} & 0 & 0 \\ 0 & e^{i\alpha_2/2} & 0 \\ 0 & 0 & 1 \end{bmatrix} \tag{1.18}$$

where c_{ij} and s_{ij} stand for $\cos(\theta_{ij})$ and $\sin(\theta_{ij})$ respectively.

Parameter	best-fit ($\pm$ 1σ)	3σ
Δm^2_{21}	$(7.54 \pm 0.24) \times 10^{-5} eV^2$	6.99 - 8.18
$\lvert\Delta m^2_{32}\rvert$	$(2.43 \pm 0.09) \times 10^{-3} eV^2$	2.19 - 2.62
$sin^2(2\theta_{12})$	0.307 ± 0.017	0.259 - 0.359
$sin^2(2\theta_{23})$	0.386 ± 0.023	0.331 - 0.637
$sin^2(2\theta_{13})$	0.0241 ± 0.0025	0.0169 - 0.0313

Table 1.2. The best current estimates for the neutrino oscillation parameters from the Particle Data Group [1]. Asymmetric standard deviations have been averaged.

The combination of measured parameters for Δm^2_{21} and $sin^2(2\theta_{12})$ is collectively known as the Large Mixing Angle (LMA) solution. The best estimates for these parameters are summarized in Table 1.2.

All of the solar neutrinos are produced in the electron flavor eigenstate. We are therefore interested in the probability of an electron neutrino transitioning to a muon or tau neutrino. The maximum energy of a solar neutrino is about 20 MeV which is below the mass of both the muon and tau. This means that solar neutrino experiments cannot distinguish between muon and tau neutrinos. The probability for an electron neutrino eigenstate to transition to either of the other flavor eigenstates is:

$$P(\nu_e \rightarrow \nu_{\mu,\tau}) = 1 - P(\nu_e \rightarrow \nu_e) \equiv 1 - P_{ee} \tag{1.19}$$

where P_{ee} is known as the electron neutrino survival probability. By using Eq. 1.16 and the parameterization from Eq. 1.18 we can write P_{ee} as:

$$
\begin{aligned}
P_{ee} =& \sum_i \sum_j |z_{\alpha\beta ij}| \, cos(\frac{\Delta m^2_{ij}}{2\bar{p}} L) \\
=& 1 - cos^4(\theta_{13}) sin^2(2\theta_{12}) sin^2(\frac{\Delta m^2_{21}}{2\bar{p}} L) \\
& - cos^2(\theta_{12}) sin^2(2\theta_{13}) sin^2(\frac{\Delta m^2_{31}}{2\bar{p}} L) \\
& - sin^2(\theta_{12}) sin^2(2\theta_{13}) sin^2(\frac{\Delta m^2_{32}}{2\bar{p}} L)
\end{aligned} \tag{1.20}
$$

where we have dropped the CP violating terms.

We now investigate the characteristic wavelengths associated with this survival probability. If we take the neutrinos to be relativistic and we approximate $\bar{p} \sim \bar{E}/c$ and plug in the missing factors of c and $\hbar$ we get $\lambda_{ij} \equiv 4\pi \bar{E}\hbar/\Delta m^2_{ij} c^3$. If we consider a 0.100 keV neutrino that is typical of the *pp* spectrum we find:

$$
\lambda_{ij} \equiv 4\pi\hbar c \frac{\bar{E}}{\Delta m^2_{ij} c^4} \sim (2.48) \frac{E[MeV]}{\Delta m^2_{ij}[eV^2]} m \tag{1.21}
$$

$$
\lambda_{21} \sim 3.24 \text{ km (at 0.100 MeV)} \tag{1.22}
$$

$$
\lambda_{31} \sim \lambda_{32} \sim 100 \text{ m (at 0.100MeV)} \tag{1.23}
$$

The region of the Sun where nuetrinos are produced is roughly $0.2R_\odot \sim 1.4 \times 10^5 \; km \gg \lambda_{ij}$. Thus, the neutrinos produced in different regions are in different phases when they arrive at Earth and the transition probabilities average out. For solar neutrino experiments, the electron neutrino survival probability is:

$$
P_{ee} = 1 - \frac{1}{2} cos^4(\theta_{13}) sin^2(2\theta_{12}) - \frac{1}{2} sin^2(2\theta_{13} \tag{1.24}
$$

$$
= cos^4(\theta_{13})(1 - \frac{1}{2} sin^2(2\theta_{12})) + sin^4(\theta_{13}) \tag{1.25}
$$

$$
\sim 0.565 \, (\theta_{13} = 0) \tag{1.26}
$$

Solar ν Species	Flux at Earth(ϕ) in $10^8 cm^{-2}s^{-1}$	
	High Z(GS98)	Low Z(AGSS09)
pp	598 ± 4	603 ± 4
^7Be	50.0 ± 3.5	45.6 ± 3.2
pep	1.44 ± 0.02	1.47 ± 0.02
^8B	0.056 ± 0.008	0.046 ± 0.006
Hep	$(8.0 \pm 2.4) \times 10^{-5}$	$(8.3 \pm 2.5) \times 10^{-5}$
^{13}N	2.96 ± 0.41	2.17 ± 0.30
^{15}O	2.23 ± 0.33	1.56 ± 0.23
^{17}F	0.055 ± 0.009	0.034 ± 0.005
CNO	5.23 ± 0.73	3.37 ± 0.52

Table 1.3. Listed above are the Solar neutrino fluxes on Earth for two different values for the metallicity parameter (Z). Metallicity is a measurement of the solar abundances of heavy elements. Figure adapted from [2] Table 2.

Thus far we've assumed that the neutrinos are propagating through a vacuum. The presence of dense matter in the Sun alters these parameters due to interactions with the surrounding particles. The leptonic matter consists entirely of electrons. This means that a ν_μ or ν_τ can only interact via the neutral current interaction but a ν_e will interact through both the charged and neutral current interactions. Since ν_es will interact more often than neutrinos of the other flavors, there is an addtional phase difference between the flavor eigenstates that leads to oscillations that are modified from the pure LMA solution. This effect is known as the Mikheyev-Smirnov-Wolfenstein (MSW) effect [15] [16]. The electron neutrinos that remain after the combination of matter enhanced effects in the Sun and neutrino oscillations through the vacuum of space as they reach Earth can be assigned a single survivability probability P_{ee}. The discovery by the Homestake experiment that this value was less than 1.0 lead to the "solar neutrino problem", a deficit of electron neutrinos from what the Standard Model predicts (see Figure 1.3) [17].

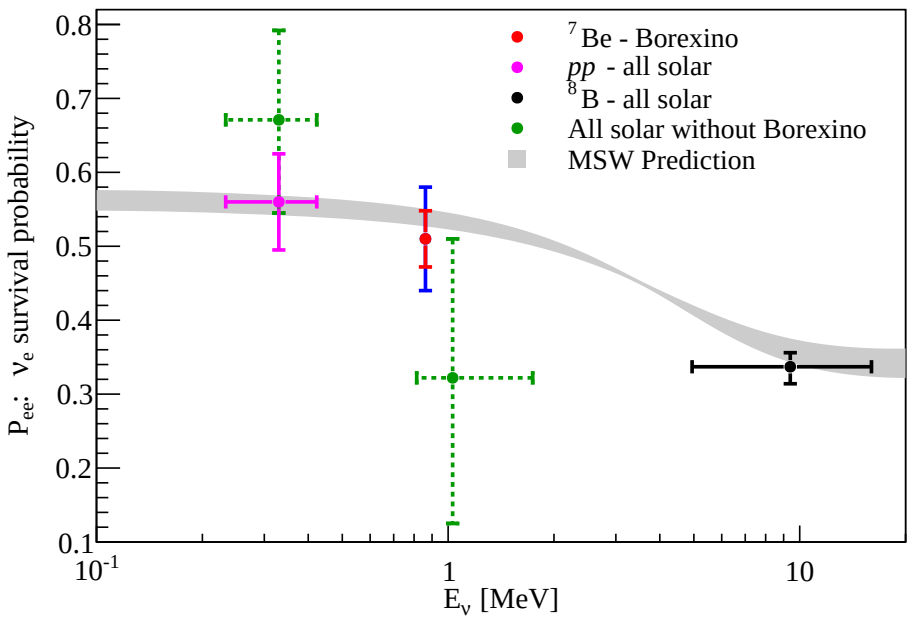

Figure 1.3. The global experimental constraints on the low energy solar electron neutrino survival probability (P_{ee}). For the ^7Be point, the inner (red) error bars show the experimental uncertainty of Borexino's precision measurement, [6] while the outer (blue) error bars show the total (experimental + SSM) uncertainty. The remaining points were obtained following the procedure in [7], wherein the survival probabilities of the low energy (pp), medium energy, and high energy (^8B) solar neutrinos are obtained, with minimal model dependence, from a combined analysis of the results of all solar neutrino eperiments. To illustrate Borexino's effect on the low energy P_{ee} measurements, the green (dashed) points are calculated without using Borexino data. The MSW-LMA prediction is also shown for comparison; the band defines the 1 - σ range of the mixing parameter estimates in [1].

Radiochemical Expiremental Results		
Experiment	$^{37}Cl \rightarrow^{37} Ar(SNU)$	$^{71}Ga \rightarrow^{71} Ge(SNU)$
Homestake [17]	$2.56 \pm 0.16(stat) \pm 0.16(sys)$	-
GALLEX [18]	-	$77.5 \pm 6.2^{+4.3}_{-4.7}$
GNO [19]	-	$62.9^{+5.5}_{-5.3} \pm 2.5$
SAGE [20]	-	$65.4^{+3.1+2.6}_{-3.0-2.8}$
SSM [BPS08(GS)] [21]	$8.46^{+0.87}_{-0.88}$	$127.9^{+8.1}_{-8.2}$

Table 1.4. Radiochemical solar-neutrino experimental results as well as the predictions of Standard Solar Model BPS08(GS). For each entry the first error is statistical contribution and the second is the systematic. A SNU(Solar Neutrino Unit) is defined as 10^{-36} neutrino captures per atom per second and is the normal unit used in radiochemical neutrino experiments. [1]

1.4 Influential Solar Neutrino Experiments

There has been no prior direct detection of the *pp* solar neutrino flux, but there have been experiments that have produced results relevant to its direct detection. Past experiments have used radiochemical detectors of chlorine (Homestake) and gallium (SAGE, GALLEX, and GNO), or water Cherekov detectors using heavy (SNO) and light water (Kamiokande and Super-Kamiokande (Super-K)) [1]. These experiments are described briefly below and their results summarized in Table 1.4.

The Homestake experiment was the first experiment to detect solar neutrinos. It proved the existance of fusion in the Sun and was the first experiment to measure a deficit in the number of expected neutrinos. This experiment relied on the neutrino capture reaction

$$\nu_e +^{37} Cl \rightarrow^{37} Ar + e^-. \tag{1.27}$$

This method takes advantage of the energy from ^{8}B neutrinos to feed a super allowed state of the ^{37}Ar that lies 5.15 MeV above the ground state. Importantly, the detection

energy threshold for this reaction, 814 keV, is above the energy of *pp* solar neutrinos. [17]

The next series of radiochemical experiements relied on the Gallium caputure reaction

$$\nu_e +^{71} Ga \rightarrow^{71} Ge + e^-. \tag{1.28}$$

This reaction has an energy threshold of 233 keV and is senstive to the *pp* solar neutrinos, however these experiments measured the integrated rate of all species above the threshold. The first of these expiriments was SAGE. Its detector consisted of 50 tons of gallium metal and published its last result in 2009 [20]. The next experiment, GALLEX, used a 100-ton gallium chloride target solution (30.3 tons of gallium) [18] to collect data over six years. Following detector upgrades, GALLEX continued operations as the Gallion Neutrino Observatory (GNO) [19]. Data-taking continued until 2003 and the sum of these gallium results provide an invaluble record of low energy solar neutrinos over a long time period.

The major solar neutrino water Cherenkov detectors are Kamiokande [22], Super-K [23], and SNO [24]. These experiments differ in a number of ways from the radiochemical ones. The most significant difference is that the neutrino interactions are all detected in real time and can make use of the relationship between the direction of the incident neutrino and the recoil electron. The high detection threshold of these experiments allows them to only measure the ^8B solar neutrinos. The results of these experiments are summarized in Table 1.5 [1].

Previous experiments were unable to directly detect the interaction rate of *pp* solar neutrinos either due to their detection threshold or the inability to separate the total flux into their spectral components. However, an estimate can be made using the sum of these experiments and the results from Borexino about the rates of these higher energy species. A global fit finds the electron neutrino *pp* flux at Earth to be $\phi_{pp}^{\oplus} = 3.38(1^{+0.14}_{-0.14}) \times 10^{10}/(cm^2 s)$ [20].

Water Cherenkov	Expiremental Results	
Experiment	Interaction	^{8}B ν flux$\pm stat \pm sys$ ($10^6 cm^{-2} s^{-1}$)
Kamiokande [22]	νe	$2.80 \pm 0.19 \pm 0.33$
Super-K III [23]	νe	$2.32 \pm 0.04 \pm 0.05$
SNO Phase I+II+III [24]	ϕ_B from fit to all reactions	$5.25 \pm 0.16^{+0.11}_{-0.13}$
SSM [BPS08(GS)] [21]	–	$5.94(1 \pm 0.11)$
SSM [SHP11(GS)] [2]	–	$5.58(1 \pm 0.14)$

Table 1.5. The most recent ^8B solar neutrino results from water Cherenkov real-time experiments and the predictions of two standard solar models [1].

CHAPTER 2

THE BOREXINO EXPERIMENT

The Borexino detector is described in detail in Ref. [25]. The following provides a general description and overview of the Borexino detector as well as the details relevant to this analysis. Borexino is a large-volume liquid-scintillator detector whose primary goal is the real-time measurement of low energy neutrinos scattering off electrons in a large scintillator volume. Located deep underground, at $\simeq$ 3800 m water equivalent (m w.e.), in the Hall C of the Laboratori Nazionali del Gran Sasso (Italy), it benefits from a suppression in the muon flux factor of $\approx 10^6$ from the earth's surface.

The main technical challenge of Borexino was the successful achievement of extremely low radioactive contamination below the neutrino interaction rate of 50 counts per day per 100 tonnes (cpd/100 t). The design of Borexino is based on the principle of graded shielding, with the scintillator at the center of concentric shells of increasing radiopurity. Every component and material used in construction was screened and selected for low radioactivity [26], and the scintillator and buffers were purified at the time of filling [27] [28]. If we assume secular equilibrium in the uranium and thorium decay chains, the Bi-Po delayed coincidence rates in the fiducial volume of Borexino imply ^{238}U and ^{232}Th levels of $(1.67 \pm 0.06) \times 10^{-17}$ g/g and, $(4.6 \pm 0.8) \times 10^{-18}$ g/g, respectively, one to two orders of magnitude lower than the original design goals of Borexino [6]. A schematic depiction of the detector can be found in Figure 2.1.

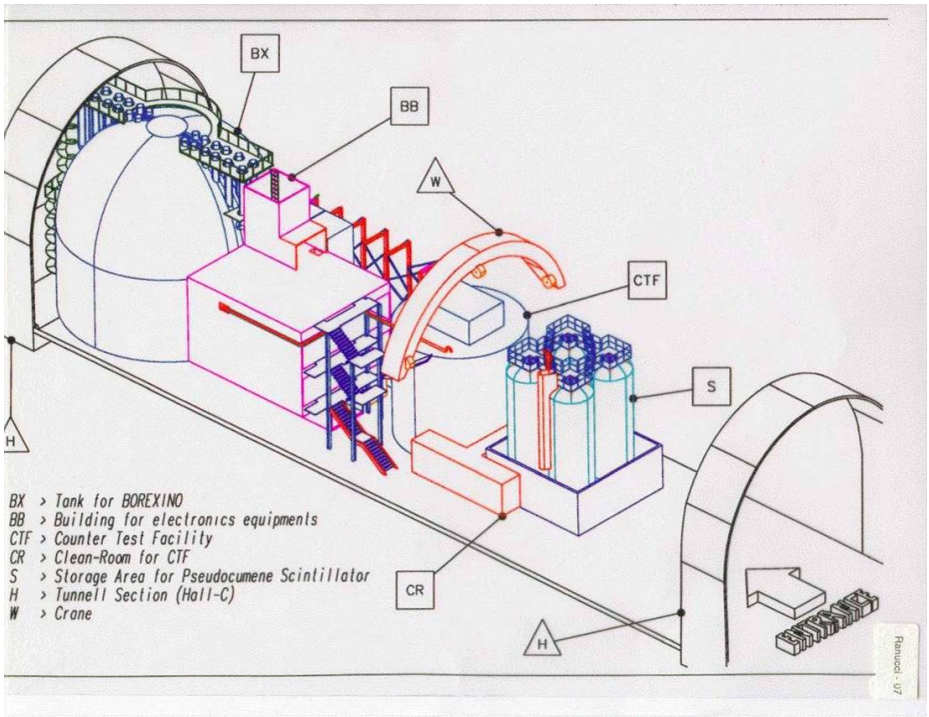

Figure 2.1. Schematic drawing of Hall C in LNGS, OPERA is now located in the Tunnell(sic) Section of the hall.

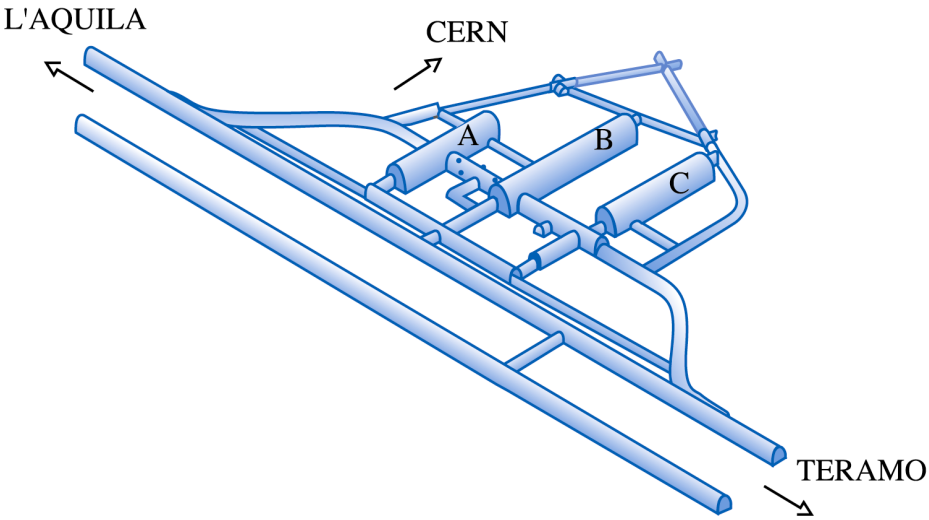

Figure 2.2. Drawing of the LNGS tunnel system. L'Aquila and Teramo are the two nearby cities on the highway off of which the lab has been build

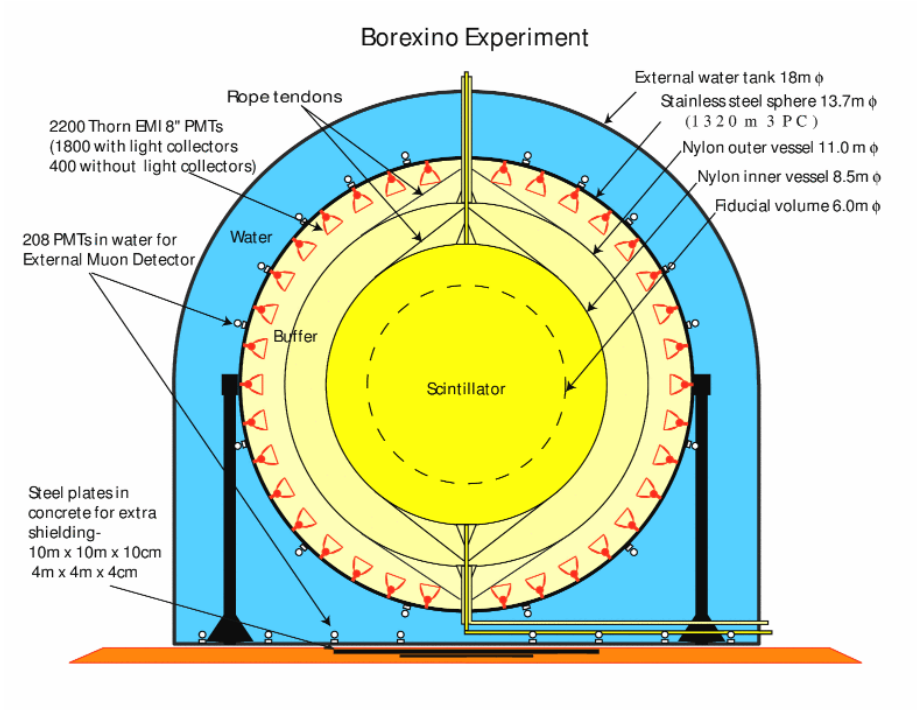

Figure 2.3. The Borexino detector with it's onion-like structure of fluid volumes with increasing radiological purity towards the center of the detector. Solar neutrino measurements are made using events that occur inside the innermost virtual volume of scintillator (fiducial volume). The large surrounding mass is necessary to shield and properly measure environmental radioactivity. The inner detector (ID) consists of all elements inside the stainless steel sphere(SSS) whereas the outer detector are the components outside of SSS but inside the water tank (WT).

2.1 Detector

The detector consists of two primary regions separated by a stainless steel sphere (SSS), the Inner Detector and the Outer Detector (see Figure 2.1).

2.1.1 Outer Detector

Despite the reduction of the muon flux provided by the rock shielding, high energy muons from cosmic ray interactions in the atmosphere still penetrate to the depth of the LNGS Hall C. These particles constitute a relevant background source for the experiment as a whole and must be tagged efficiently for the success of the Borexino

physics program [25]. The Outer Detector (OD) plays a key role in the methods used to tag the high energy muon background.

The outside enclosure is the Water Tank (WT), consisting of a cylindrical base with a 18m diameter and a hemispherical top with a maximum height of 16.9 m. When filled, the tank acts as a powerful shield against external backgrounds (neutrons and γrays from the surrounding rock) as well as a Cherenkov muon counter and tracker. The muon flux is reduced by a factor of 10^6 after passing through the 3800m w.e. depth of the Gran Sasso Laboratory, resulting in a residual flux on the order of 1 $m^{-2}h^{-1}$. This rate integrates to about 4000 muons per day crossing the detector. If undetected, this flux is still well above the needs of Borexino and an additional reduction factor of about 10^4 is provided by the Outer Detector(OD).

The OD is a water Cherenkov detector consisting of 208 photomultiplier tubes (PMTs) installed the Water Tank (WT), a volume filled with ultra-clean water that serves a dual role in providing additional shielding for the rest of the experiment as well as a light source for high-energy charged particles. The majority of the PMTs are located on the outer surface of the Stainless Steel Sphere (SSS), placed in 12 horizontal rings, with every PMT facing radially outward. The lowest quarter of these are actually repositioned onto the floor of the WT and placed in 5 concentric circles. This was done to allow for better muon tracking as this configuration was shown to reduce the amount of reflected light collected by the PMTs, without decreasing the efficiency of the muon detection. Light collection is further maximized by a covering layer of Tyvek®, a white paper-like material with high reflectivity, placed over the interior surface of the WT.

2.1.2 Inner Detector

Supported by 20 steel legs inside the water tank sits the Stainless Steel Sphere. An unsegmented sphere that serves as both a container for the scintillator and the

mechanical support of the PMTs. Inside the sphere are two nylon vessels that separate the Inner Detector (ID) volume into three spherical shells of radii 4.25 m, 5.50 m, and 6.85 m. The inner vessel (IV) contains the liquid scintillator solution of PC (pseudocumene, 1,2,4-trimethylbenzene $C_6H_3(CH_3)_3$) as the solvent for the fluor PPO (2,5-diphenyloxazole, $C_{15}H_{11}NO$) at a concentration of 1.5 g/l (0.17% by weight). The outer two shells contain PC with 2 g/l of DMP (dimethylphthalate, $C_6H_4(COOCH_3)_2$) added as a quencher to reduce the yield of pure PC [29]. Neutrinos are detected in Borexino by the scintillation light produced by the recoiling electrons from their elastic scattering inside the inner vessel. The key to Borexino's neutrino science program has been the successful achievement of extremely low levels of radioactive contamination in all of the components of the inner detector [6].

There are a couple of important changes to the performance of the inner detector since commissioning that are worth discussion. The inner detector initially consisted of 2212 PMTs that collect the scintillation light inside the SSS. The current number of active PMTs is closer to 1700 due to the gradual loss of PMTs over the years of Borexino's operation exceeding the number of replacements that existed. This has led to a number of changes in the trigger and data selections that are discussed in Section 2.1.3.

Starting on approximately April 9th, 2008, a pinhole perforation of the inner vessel has caused scintillator from the IV to leak into the buffer region inside of the outer vessel. The initial rate was estimated to be about 1.33 m^3/month. This rate was reduced by removing DMP from the buffer by distillation. This reduced the density difference between in inner and outer vessel and thus also reduced the pressure difference accross the nylon vessel. There were a couple of purification campaigns that in the end reduced the DMP concentration to 2 g/l from 5 g/l. This concentration was still high enough to suppress scintillation in the buffer and was able to reduce the

leak rate to about 1.5 m^3/year [30]. The scintillator that was lost from the IV was replaced by several refilling operations with PC and the IV shape has since stabilized.

2.1.3 Trigger and Data Selection

Borexino detects neutrinos in real time from the light produced by the recoiling electrons. For each event, the detector records the amount of light collected by each PMT and the relative detection times of the photons. Borexino's data is broken up into 6 hour long runs that are each individually validated by a weekly shifter before being accepted for analysis. Each run is made up of many individual 16.5 μs triggers that occur at a rate of about 30 Hz. The Borexino trigger records data if the number of PMTs triggered in a 60 ns time window exceeds the Borexino Trigger Board(BTB) threshold. This threshold has been reduced to 20 from 25 to account for the reduced number of active PMTs within the detector.

The data selection and analysis cuts specific to this analysis are discussed in detail in Section 4.3. The basic data selection criteria for solar neutrino analysis are: 1) events are removed that occur in a 300 ms window after a muon has crossed the inner detector to eliminate muons and the radioactive isotopes they can produce and; 2) select only events that occur within the innermost volume of the detector to eliminate background from radioactivity in the nylon vessels and PMTs.

2.2 Previous Borexino Results

Borexino has been running for the last 6 years and many contributions have been made to the fields of particle physics and astrophysics. Highlighting just the major results of the past 6 years includes the first real time measurement of ^{7}Be solar neutrinos [31] as well as a precision measurement of their flux [6] (See Figure 2.2), measurements have been published of the solar ^{8}B neutrino interaction rate [3], and the first evidence of *pep* solar neutrinos by direct detection [32]. We were also able to

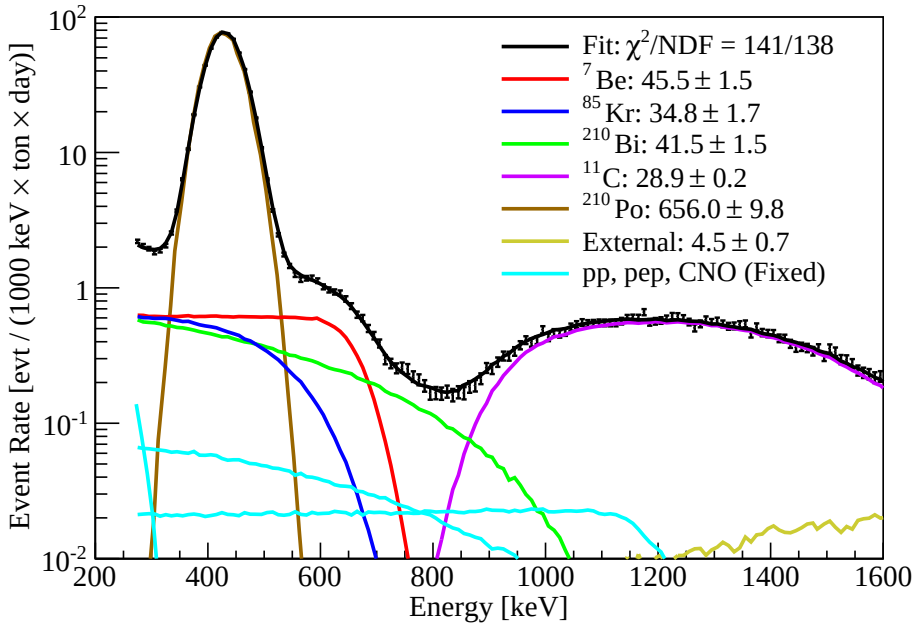

Figure 2.4. A sample fitted spectra from the precision ^{7}Be measurement [6]; the fit results in the legend have units [counts/(day x 100 ton)] and the fit was performed over the energy region of 270 to 1600 keV. The processes to produce these kinds of results are described in Section 4.4.

make the first observation of geo-neutrinos at more than 3σ C.L. originating from radioactive isotopes (U, Th) in the Earth [33]. Additionally, Borexino participated in a program to measured the speed of neutrinos from CERN showing that they are subluminal, as predicted by Special Relativity [34]. Borexino is also a member experiment of the Super Nova Early Warning System(SNEWS), a multi-experiment collaboration that aims to provide early warning of any galactic supernovae for astronomers [35].

Recently Borexino underwent a large and rigorous purification campaign that resulted in the reduction of many internal background sources [36]. The reduction of these background levels to even lower contamination levels has presented the first experimental environment suitable for the measurement of the *pp* solar neutrino spectrum.

CHAPTER 3

SIGNALS AND BACKGROUNDS

Neutrinos are detected in Borexino due to their elastic scattering off of electrons, protons, and neutrons in the detector. The maximum imparted energy occurs in a neutrino backscatter and can be calculated as:

$$T_{max} = \frac{2E_\nu}{mc^2 + 2E_\nu} \cdot E_\nu \tag{3.1}$$

For electrons and protons the energy goes directly into the ionization of the scintillator molecules where as the neutrons must first collide with the protons in the detector. Due to the mass of neutrons and protons the recoil energy is much less than that of electrons and even the most energetic solar neutrino recoils are placed below our detection threshold by an order of magnitude. The expected spectrum for the various solar species as seen by Borexino can be viewed in Figure 3.1

Borexino is uniquely prepared to directly measure the lowest energy neutrino in the proton-proton chain, the *pp* neutrino itself. The ultra-pure nature of the components used in its construction as well as its use of a liquid scintillator allow it to achieve a much lower energy threshold for neutrino detection than previous detectors. The use of a liquid scintillator allows for a low energy threshold while the high radio purity allows the detector to measure faint signals. The first direct measurement of solar neutrinos below 250 keV is an accomplishment in itself and it's also important to note that the ppI branch of the *pp* chain in the Sun has yet to be directly detected. Their detection provides a fundamental verification of the Standard Solar Model. This chapter will discuss the expected signal from the *pp* solar neutrinos and the

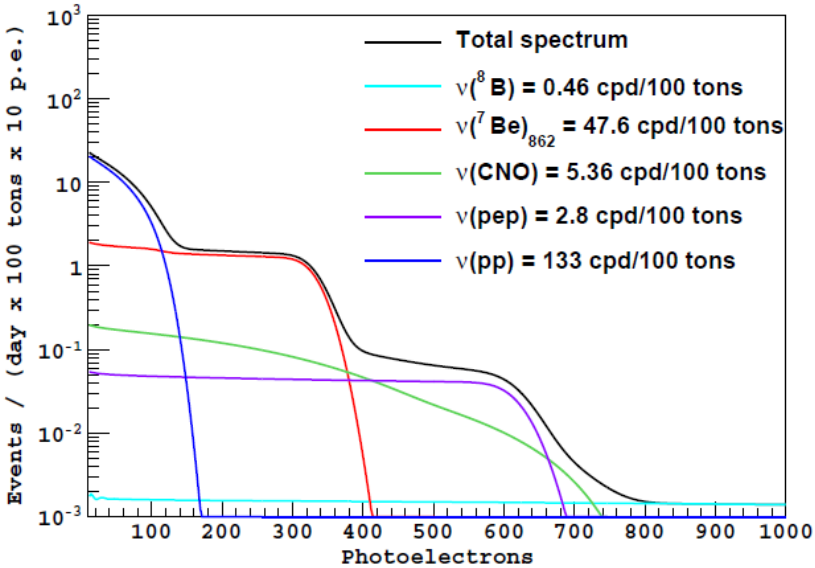

Figure 3.1. Simulated energy spectra (including detector response) for electron recoil of solar neutrinos in Borexino. The production rates were fixed to the SSM prediction for the LMA-MSW solution using oscillation parameters in [1]. Energy is displayed as the number of detected photoelectrons. One photoelectron corresponds to approximately 2keV of energy deposited in the detector.

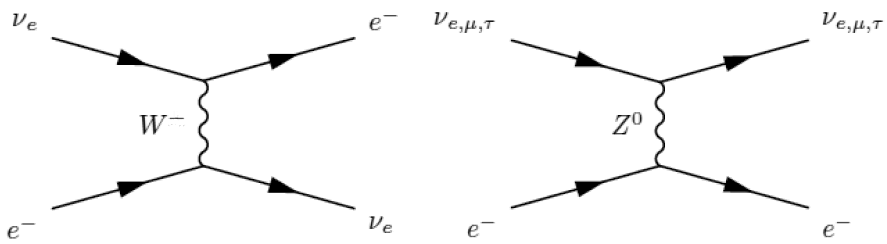

Figure 3.2. Feynman diagrams to first order for neutrino-electron elastic scattering. Left: Charged-current interaction via the exhange of a charged W boson. Right: Neutral-current interaction via the exchange of a Z^0 boson.

backgrounds in Borexino that must be understood for this measurement. It will also touch on the other backgrounds in Borexino that may have been important in other results and explain why they were not a significant source of concern for this result.

3.1 Neutrino-Electron Elastic Scattering

Neutrinos can scatter off of electrons through either the charged or neutral current interactions. Neutral current scattering (shown on the right of Figure 3.1) is open to all neutrino flavors. However, only electron neutrinos can scatter off electrons via the exchange of a W boson (left of Figure 3.1). The differential cross section (to first order, ignoring radiative corrections), to produce a recoiling electron with kinetic energy T due to scattering with a neutrino of energy E_ν is:

$$\frac{d\sigma_\nu}{dT}(E_\nu, T) = \frac{\sigma_0}{m_e c^2}[g_L^2 + g_R^2(1 - \frac{T}{E_\nu})^2 - g_L g_R \frac{m_e c^2 T}{E_\nu^2}] \tag{3.2}$$

where

$$\sigma_0 = \frac{2G_F^2 m_e^2}{\pi \hbar^4} = 8.806 \cdot 10^{-45} cm^2, \tag{3.3}$$

$g_L = sin^2\theta_W \pm \frac{1}{2}$, and $g_R = sin^2\theta_W \simeq 0.23$, where θ_w is the electroweak mixing angle.

3.2 *pp* Neutrinos

The interaction rate of *pp* neutrinos, per target mass, can be expressed as:

$$R = \Phi\ n \int S_\nu(E)(P_{ee}(E)\sigma_{\nu_e}(E) + (1 - P_{ee})\sigma_{\nu_{\mu\tau}}(E))dE \tag{3.4}$$

where $S_\nu(E)$ is the *probability density function*(pdf) of the neutrino, the integral is performed over the *pp* neutrino energy range, Φ is the flux, P_{ee} is the electron neutrino survival probability(see Eq. 1.20), and σ_{ν_e} and $\sigma_{\nu_{\mu\tau}}$ are cross sections for electron neutrinos and muon or tau neutrinos respectively with the electrons in the scintillator. The cross section for ν_e is larger than for the other two flavors across the entire energy range in Borexino (for *pp* neutrinos $\sigma_{\nu_{\mu,\tau}} \simeq 3.3 \times 10^{-46} cm^2$, $\sigma_{\nu_e} \simeq 11.6 \times 10^{-46} cm^2$ [37]). This is because they are able to interact via both charged and neutral current interactions instead of just neutral interactions as is the case for the flavors of the heavier leptons. Figure 3.2 shows these cross sections as a function of neutrino energy.

The electron density in the scintillator is $n = (3.307 \pm 0.003) \times 10^{31}/(100\ \text{t})$. When integrated over the appropriate values for the *pp* spectrum (0-0.42 MeV) we get an expected detection rate of 132.9 ± 1.9 cpd/100 t in the high-metalicity Standard Solar Model (GS98) and 133.2 ± 1.9 cpd/100 t for the low-metalicity model (AGSS090) [30]. The spectral distribution of this rate was shown in Figure 3.1 and Table 3.1

3.3 Backgrounds

The low level of backgrounds in Borexino has been the most important factor in its ability to produce new solar neutrino measurements [30]. This section describes the major background sources critical to the measurement of the *pp* result. These backgrounds can be divided into three major categories: external and surface backgrounds are those that are generated outside the scintillator or as a result of

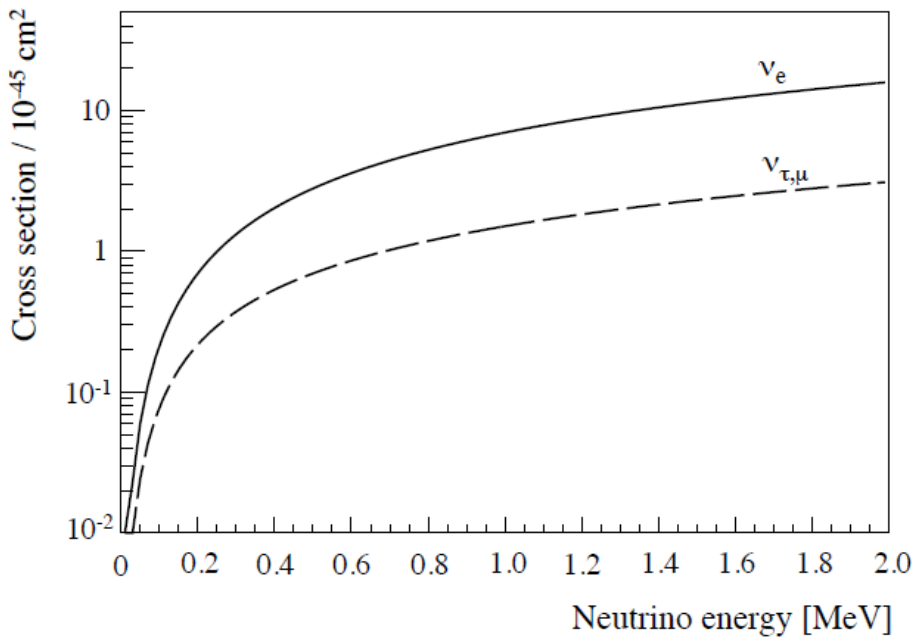

Figure 3.3. The cross section for neutrino-electron elastic scattering as a function of neutrino energy. The *pp* neutrino spectrum lies between 0 and 0.42 MeV.

Solar ν	GS98 Flux High metallicity $[cm^{-2}s^{-1}]$	AGSS09 Flux Low metallicity $[cm^{-2}s^{-1}]$	e^- recoil end point [MeV]	GS98 rate [cpd/100 t]	AGSS09 rate [cpd/100 t]	Main background
pp	$5.98(1 \pm 0.006) \times 10^{10}$	$6.03(1 \pm 0.006) \times 10^{10}$	0.26	132.9 ± 1.9	133.2 ± 1.9	^{14}C
^7Be	$5.00(1 \pm 0.07) \times 10^9$	$4.56(1 \pm 0.07) \times 10^9$	0.66	48.5 ± 3.7	44.0 ± 3.2	$^{85}Kr, ^{210}Bi$
pep	$1.44(1 \pm 0.012) \times 10^8$	$1.47(1 \pm 0.012) \times 10^8$	1.22	2.75 ± 0.05	2.81 ± 0.05	$^{11}C, ^{210}Bi$
^{13}N	$2.96(1 \pm 0.14) \times 10^8$	$2.17(1 \pm 0.14) \times 10^8$	1.19			
^{15}O	$2.23(1 \pm 0.15) \times 10^8$	$1.56(1 \pm 0.15) \times 10^8$	1.73			
^{17}F	$5.52(1 \pm 0.17) \times 10^6$	$3.40(1 \pm 0.16) \times 10^6$	1.74			
CNO	$5.24(1 \pm 0.21) \times 10^8$	$3.76(1 \pm 0.21) \times 10^8$	1.74	5.26 ± 0.52	3.78 ± 0.39	$^{11}C, ^{210}Bi$
^8B	$5.58(1 \pm 0.14) \times 10^6$	$4.59(1 \pm 0.14) \times 10^6$	17.72	0.44 ± 0.06	0.36 ± 0.05	^{208}Tl, ext γ

Table 3.1. The flux, electron recoil end point, interaction rate, and main backgrounds for solar neutrinos in Borexino.

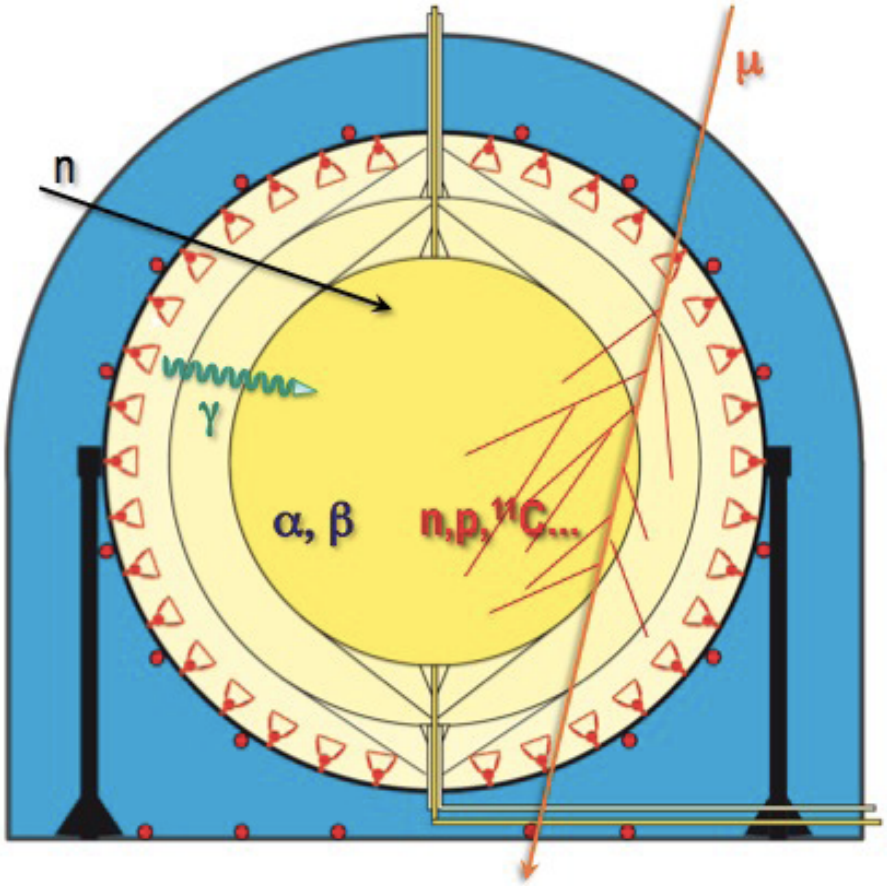

Figure 3.4. Illustration of the potential internal, external and cosmogenic background sources in Borexino. In green are external gammas from radioactivity in the SSS, PMTs, and nylon vessels. Shown in red are cosmic muons and the cosmogenic backgrounds that can result from their passage through the scintillator. Depicted in blue are internal alphas and betas from radioactive decays inside the scintillator.

contaminants on the surface of the nylon IV, internal backgrounds are those that are a result of contaminants in the scintillator itself, and finally cosmic muons and the radioisotopes that are produced as a result of their passage through the detector form the cosmogenic backgrounds.

3.3.1 External and Surface

The primary source of external backgrounds are radioactive decays in the hardware that surrounds the scintillator [6]. The external and surface backgrounds in Borexino are minimized by the careful selection of the fiducial volume (FV) within the scintillator. The position reconstruction of events allows the selection of a FV that reduces the contribution of these external backgrounds to a negligible level.

3.3.2 Internal

Internal backgrounds consist of those events that can be separated from the signal only through their spectral shapes or through their proximity to a cosmogenic event. In the following we discuss the background sources, lifetimes and spectral shapes. Figure 3.3.2 shows the expected energy spectrum of the background species and neutrinos after detector effects in Borexino.

The largest internal background source is ^{14}C. The ^{14}C isotope is a β^- emitter with a 0.156 MeV end point and a half-life of 5730 years. It is produced in the upper atmosphere via the interaction of thermalized cosmogenic neutrons with nitrogen through the reaction ^{1}n + ^{14}N $\rightarrow$^{14}C + ^{1}p. In order to reduce the levels of contamination the scintillator in Borexino is derived from petroleum from deep underground where the ^{14}C levels are reduced by a factor of about a million from the surface where it's being continuously replenished by the cosmic ray flux. Despite the minuscule isotopic fraction of 3×10^{-18} ^{14}C/^{12}C in the scintillator, ^{14}C is still responsible for the vast majority of the trigger rate in Borexino and determines the low energy threshold

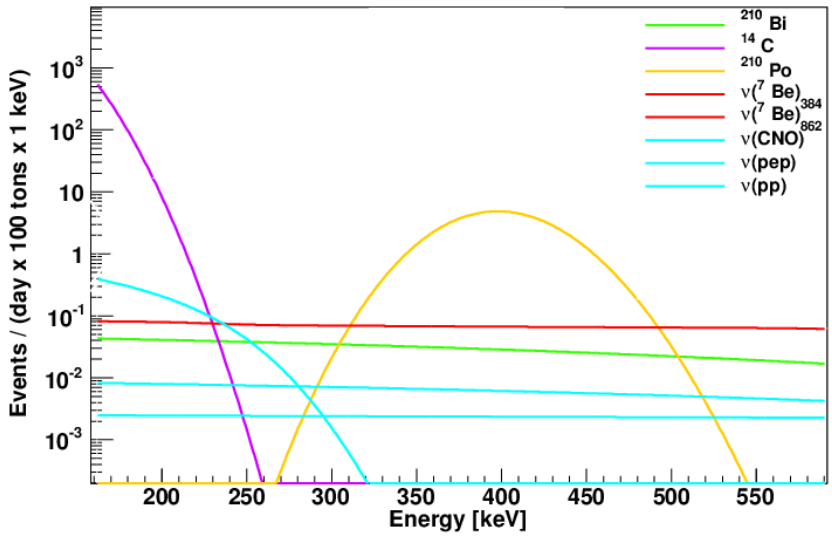

Figure 3.5. Expected energy spectrum in Borexino for solar neutrinos and the relevant background sources including all detector effects applicable to the *pp* analysis.

Isotope	Mean Life	Energy[MeV]	Decay
^{238}U	6.45 x 10^9 yrs	4.20	α
^{234}Th	34.8 days	0.199	β^-
^{234m}Pa	1.70 min	2.29	β^-
^{234}U	3.53 x 10^5 yrs	4.77	α
^{230}Th	1.15 x 10^5 yrs	4.69	α
^{226}Ra	2.30 x 10^3 yrs	4.79	α
^{222}Rn	5.51 days	5.49	α
^{218}Po	4.40 min	6.00	α
^{214}Pb	38.7 min	1.02	$\beta^-\gamma$
^{214}Bi	28.4 min	3.27	$\beta^-\gamma$
^{214}Po	236 μs	7.69	α
^{210}Pb	32.2 yrs	0.063	$\beta^-\gamma$
^{210}Bi	7.23 days	1.16	β^-
^{210}Po	200 days	5.41	α
^{206}Po	stable	-	-

Table 3.2. The decay chain of ^{238}U with lifetimes, maximum released energies and decay type. Relevant to the *pp* analysis are the betas and alphas from ^{210}Bi and ^{210}Po due to both their energies and the presence of 210Pb disolved in the scintillator.

of the measurement. The hardware trigger threshold of ~ 50 keV reduces the rate to approximately 30 counts per second from several hundred counts per second.

The rest of the relevant internal backgrounds are due to the ^{238}U chain and ^{222}Rn(see Table 3.2). The two isotopes that remain relevant to our analysis are ^{210}Bi and ^{210}Po. ^{210}Bi is one of the dominant backgrounds for the ^{7}Be neutrino analysis [6]. It is a β^- emitter with an end point of Q = 1.16 MeV and a mean life of 7.23 days. ^{210}Po is an α emitter with an end point of 5.41 MeV and a mean life of 200 days. Like all α's, these events are quenched by a factor of ~ 10 with respect to the energy of β events.

3.3.3 Muon and Cosmogenic

Radioactive isotopes can be produced *in situ* due to the passage of muons through the scintillator in the inner detector. ^{11}C is the dominant cosmogenic background in Borexino after cuts with a residual rate of $28.5 \pm 0.2 \pm 0.7$ cpd/100 tons due to its relatively long lifetime [6]. Though one of the primary challenges of the *pep* and CNO ν measurements [32] its spectral contribution lies above the *pp* ν fit range and for the *pp* only the muons themselves matter. Muons and the other cosmogenic isotopes are reduced to negligible levels by the 300ms veto that is applied after every muon(see Section 4.3). The isotopes, their energy and rates after this cut are show in Table 3.3.

3.3.4 ^{14}C Pileup

The background that the *pp* result is most sensitive to is the pileup of ^{14}C with itself. From Figure 3.3.2 we can see that the sum of two events in the ^{14}C spectrum can result in a combined energy similar to that of a *pp* event. The length of the trigger window in Borexino is long ($\sim 16.5\mu$ s) with respect to the typical length of a scintillation event ($\sim 1\mu$ s). A situation can arise where two distinct physical events

Isotope	Mean Life	Energy and Decay [MeV]	Residual rate [cpd/100 tons]
n	255μs	2.22 γ capture on ^{1}H	< 0.005
^{12}N	15.9ms	17.3 β^+	< 5 x 10^{-5}
^{13}B	25.0ms	13.4 $\beta^-\gamma$	< 5 x 10^{-5}
^{12}B	29.1ms	13.4 β^-	(7.1$\pm$0.2) x 10^{-5}
^{8}He	171.7ms	10.7 $\beta^-\gamma n$	0.004 ± 0.002
^{9}C	182.5ms	16.5 β^+	0.020 ± 0.006
^{9}Li	257.2ms	13.6 $\beta^-\gamma n$	0.022 ± 0.002
^{8}B	1.11s	18.0 $\beta^+\alpha$	0.21 ± 0.05
^{6}He	1.16s	3.51 β^-	0.31 ± 0.04
^{8}Li	1.21s	16.0 $\beta^-\alpha$	0.31 ± 0.05
^{11}Be	19.9s	11.5 β^-	0.034 ± 0.006
^{10}C	27.8s	3.65 $\beta^+\gamma$	0.54 ± 0.04
^{7}Be	76.9 days	0.478 $EC\gamma$	0.36 ± 0.05

Table 3.3. Cosmogenic isotopes in Borexino. The final column shows the expected residual rates after the 300ms time veto that is applied following each muon (see Section 4.3). The total rates have been evaluated following [3] or by extrapolating FLUKA simulations reported in [4].

can occur in the same trigger gate and the PMT hits overlap. Due to the importance of this species its been given its own chapter (see Chapter 5).

CHAPTER 4

ANALYSIS METHODS

The output of Borexino for analysis consists of $\sim$ 6 hour data runs made up of about half a million triggers (refer to Subsection 2.1.3 for a discussion of the trigger system). Each of these triggers contains the raw data from all of the PMTs and other detector components. This data must first be processed into a form that contains meaningful information about the reconstructed events in the trigger.

4.1 Event Reconstruction

The reconstruction of an event in Borexino can be broken down into a number of distinct stages. The initial stage is collectively referred to as "low level analysis". Following this is clustering, position reconstruction, energy reconstruction, pulse shape discrimination, and muon track reconstruction.

Low level reconstruction is the conversion of the raw detector data into the three main pieces of information about each PMT hit: the timing, amount of light collected (charge) expressed as number of photoelectrons(p.e.'s), and position of the hit PMT. This information is used in all of the following phases of reconstruction. Due to historical reasons, after the low level analysis the reconstruction code branches into two different analysis frameworks: Echidna and MOE (*Mach4* Over Echidna). In the end, the information from both codes is combined in the final analysis and their relative agreement is assessed.

4.1.1 Clustering

As mentioned previously, the length of the trigger gate is 16.5 μs. However, the typical time range of a single event in Borexino is $\sim$1 μs. Clustering is the process by which we assign each hit in a given trigger to either a coincidental dark noise hit or to one of the possible physical events during that time frame. Those hits that are clustered together as coming from the same interaction in the detector are then used in the position and energy reconstruction for that event. The efficiency of this clustering is one of the major concerns for the handling of pileup in the detector. If we were able to separate all events inside our detector with 100 percent efficiency then there wouldn't be any pileup. This is also one of the driving factors for the selection of an energy variable (see Section 4.2).

The precise method of clustering is different between the two branches of the analysis code but the overarching principle is the same. This section details the methods used in the MOE algorithms. Initially, all valid hits are binned in a histogram with a bin width of 16 ns. The start of a cluster is identified when the number of hit PMTs (hits) in a window of length w_{start} exceeds the noise threshold of the event by a given amount. The end of the cluster is defined when the number of hits in a window of length w_{end} drops below a given threshold above the noise level. The final step is to ensure that there are at least 20 hits included in the cluster and if not, discard it. If there are more than 20 total hit PMTs, then all of the hits that occured between the time where w_{start} was identified and the time where w_{end} was found are collected into a cluster and fed into the rest of the reconstruction algorithm.

4.1.2 Energy Reconstruction

There are two main types of energy estimators used by Borexino results. NPMTs is based on the number of PMTs hit in a specific time window after the start of the cluster and NPE or charge is based on the total charge recorded by the PMTs.

This analysis uses an NPMTs based variable and we restrict our discussion to these variables. A discussion on other estimators can be found in [30]. This analysis uses two energy variables, npmts_dt1 and npmts_dt2, which differ in the length of time after the cluster start is identified during which PMT hits are included. For npmts_dt1, all PMTs are included in a 230ns window after the cluster start; for npmts_dt2 this window is 400ns. The motivations for these variables and their relationship to the true energy are discussed in Section 4.2

4.1.3 Position Reconstruction

The most important reduction technique for external backgrounds is the definition of a central fiducial volume inside the inner vessel. By reconstructing the position of each event we can reject background events originating on or near the Stainless Steel Sphere, inner/outer vessels, and their end-caps through the selection of a central fiducial volume. The algorithm used for position reconstruction determines the most likely vertex position, $\vec{r}_0$, of the interaction based on the arrival time of the photons to each PMT and their positions, $\vec{r}_j$. The algorithm finds these values by maximizing the likelihood that the event occurred at a position $\vec{r}_0$ at the time $\vec{t}_0$ by subtracting a position dependent time-of-flight from the arrival time at each PMT. [30]

4.2 Selection of Energy Estimator and its Response Function

Borexino has used both continuous (NPE or charge) and discrete (NPMTs or NHits) energy estimators. This analysis has chosen to use NPMTs primarily in order to reduce the effect of noisy PMTs in the low energy region of interest for our analysis. Our analysis is interested in a region of energy where the expected number of photons per PMT is much less than one. Because of this, we can minimize the undesired effect of a malfunctioning PMT that is behaving as if it were hit multiple times without skewing the true energy of our event. We've also chosen to use two estimators that

only consider the number of PMTs in fixed time window after the start of the cluster, 230 ns for npmts_dt1 and 400 ns for npmts_dt2. We've made this choice because the rate of pileup is directly correlates to the length of the window considered. This provides a quantitative consistancy check for our pileup methods (see Chapter 5).

Next, we discuss how we convert the energy spectra of all of the species in our detector from true energy (keV) into the energy estimator that our detector gives us (npmts_dt1(dt2)). In the following derivation we may occasionally be generous with our use of the term *probability density function* (pdf) $p(x)$. In the case of continuous variables we mean the usual $P(a \leq x \leq b) = \int_a^b p(x)dx$. However, for discrete variables, we mean $P(a \leq x \leq b) = \int_a^b (\sum_{i=1}^n p_i \delta(t - x_i))dt$, where the x_i are the permitted values of the descrete variable and the p_i are the probabilities associated with each of these values.

In order to fit our data (see Section 4.4) we must convert the energy distributions of the neutrino and background species obtained from the literature to the expected shapes in the desired energy estimator. This is done by convolving the energy distributions with an energy response function, $P(q|E)$, that is the probability distribution function for the estimator q, given an event energy E. Detailed derivations of the response function used in the ^{7}Be analysis can be found in [30]. In the context of these results we present the changes needed to handle the energy estimators used in this analysis.

We assume that the β response function in Borexino follows a generalized gamma function as previous studies have shown [30]. This function describes the detector response to recoiling electrons of a given energy and how that would look in our given energy estimator. The construction of this function requires the mean and the variance to be calculated. The following derivation [38] can be applied to both of the energy estimators used in this analysis. The differences that result from the two time windows is absorbed in the parameter Y_{det} in Eq. 4.1. The following formalism can

be used for all NPMTs-like variables and we refer to the number of PMTs that have detected at least one hit generally as N_p.

Given an event of energy E, we define the corresponding number of photoelectrons N_{pe} to be:

$$N_{pe} = Y_{det} \cdot E \cdot Q_p(E) \tag{4.1}$$

where Y_{det} is the light yield averaged over the fiducial volume, and $Q_p(E)$ is the quenching factor. We can then define the average number of photoelectrons collected by one PMT as:

$$\mu_0 = N_{pe}/N_{live} \tag{4.2}$$

where N_{live} is the number of live PMTs at the time of the event. Given that the distribution of detected photoelectrons at each PMT is expected to be Poissonian [30], the probability of having a signal at any single PMT is:

$$p_1 = 1 - e^{-\mu_0} \tag{4.3}$$

If we assume the event takes place at the center of the detector we find the mean number of PMTs hit to be:

$$N_p^{ctr} = N_{live} \cdot p_1 = N_{live} \cdot (1 - e^{-\mu_0}) \tag{4.4}$$

When extending this to events taking place in the entire fiducial volume, N_p is also a function of the position of the event. Most of the corrections are due to changes in the solid angle and has been found empirically for the ^{7}Be analysis [6] and can be extended to our analysis as the choice of fiducial volume is the same.

$$\mu_{0_{gc}} \equiv N_{pe}/(N_{pe} \cdot gc + N_{live}) \tag{4.5}$$

$$p_{1_{gc}} \equiv 1 - e^{-\mu_{0_{gc}}} \tag{4.6}$$

$$N_p = N_{live} \cdot p_{1_{gc}} \tag{4.7}$$

where gc is a geometric correction factor that accounts for the fact that events are spread throughout the entire fiducial volume. As noted earlier, the number of live PMTs varies and thus N_{live} is time-dependent:

$$\overline{N_p(t)} = \overline{N_{live}(t)} \cdot p_{1_{gc}} \tag{4.8}$$

where we have averaged over the time-dependent variables.

This is now the relation between the energy of an event and the mean value of the number of PMTs hit. The actual number of PMTs hit for given energy will have its own variance σ_{N_p}. To estimate this variance we assume that we are interested in a fixed time t_0, so that the number of live PMTs is fixed at $N_{live}(t_0)$, and only concerned with events that occur at a fixed position $\vec{r_0}$ in the fiducial volume. Given an event of energy E, we can write the probability that PMT i will be hit as $p_1^i(E, \vec{r_0})$, such that:

$$\epsilon(N_p(E, \vec{r_0}, t_0)) = \sum_{i=1}^{N_{live}(t_0)} p_1^i(E, \vec{r_0}) \tag{4.9}$$

is the expected central value of the N_p with the sum being only over live PMTs. If we make the reasonable assumption that we can treat each PMT independently, we can assume they each behave binomially and add their individual variances.

$$\sigma^2_{N_p}(E, \vec{r_0}, t_0) = \sum_{i=1}^{N_{live}(t_0)} p_1^i(E, \vec{r_0}) \cdot [1 - p_1^i(E, \vec{r_0})] \tag{4.10}$$

$$= \epsilon(N_p(E, \vec{r_0}, t_0)) - N_{live}(t) \cdot \frac{1}{N_{live}(t)} \sum_{i=1}^{N_{live}(t_0)} [p_1^i(E, \vec{r_0})]^2 \tag{4.11}$$

We note that the last term is the mean of a variable squared, and that by applying the definition of variance,

$$\sigma^2_{N_p}(E, \vec{r_0}, t_0) = \epsilon(N_p(E, \vec{r_0}, t_0)) - N_{live}(t) \cdot (\sigma_1^2(E, \vec{r_0}) + p_1^2(E, \vec{r_0})) \tag{4.12}$$

where the mean $p_1(E, \vec{r_0})$ is defined from Eq. 4.9:

$$p_1(E, \vec{r_0}) \equiv \frac{1}{N_{live}(t)} \cdot \sum_{i=1}^{N_{live}(t_0)} p_1^i(E, \vec{r_0}) = \frac{\epsilon(N_p(E, \vec{r_0}, t_0))}{N_{live}(t)} \tag{4.13}$$

Above we are assuming that $p_1(E, \vec{r_0})$, the mean probability for any given PMT to detect at least one photoelectron, and its associated variance are time-indepent. We assert that this is valid because assuming that the PMTs are distributed isotropically at all points in time is a reasonable approximation of the situation in Borexino. We now define the relative variance $v_1(E, \vec{r_0}) = \sigma_1^2(E, \vec{r_0})/p_1^2(E, \vec{r_0})$ to arrive at:

$$\sigma^2_{N_p}(E, \vec{r_0}, t_0) = \epsilon(N_p(E, \vec{r_0}, t_0)) - N_{live}(t_0) \cdot p_1^2(E, \vec{r_0}) \cdot (1 + v_1(E, \vec{r_0}))) \tag{4.14}$$

Applying Eq. 4.9 again yields,

$$\sigma^2_{N_p}(E, \vec{r_0}, t_0) = \epsilon(N_p(E, \vec{r_0}, t_0)) \cdot (1 - p_1(E, \vec{r_0}) \cdot (1 + v_1(E, \vec{r_0}))) \tag{4.15}$$

This gives the variance in a situation where all events are localized at $\vec{r_0}$ and t_0. In order to account for variations in those parameters we must calculate the grand variance $\sigma^2_{N_P}$:

$$\sigma^2_{N_P} = \overline{\left\langle \epsilon(N_p^2(E, \vec{r}, t)) \right\rangle} - \overline{\langle \epsilon(N_p(E, \vec{r}, t)) \rangle}^2 \tag{4.16}$$

where $\langle\rangle$ denotes the average of the variable over the entire fiducial volume and the bar denotes an average over time. We can expand the first term on the right hand side to get the following:

$$\sigma^2_{N_P} = \overline{\left\langle \sigma^2_{N_P}(N_p^2(E, \vec{r}, t)) + \epsilon^2(N_p^2(E, \vec{r}, t)) \right\rangle} - \overline{\langle \epsilon(N_p(E, \vec{r}, t)) \rangle}^2 \tag{4.17}$$

where $\sigma^2_{N_P}(N_p^2(E, \vec{r}, t))$ is now purely the statistical variance of Eq. 4.15. This allows us to write:

$$\sigma^2_{N_P} = \overline{\langle \epsilon(N_p(E, \vec{r}, t))[1 - p_1(E, \vec{r})(1 + v_1(E, \vec{r})] \rangle} \tag{4.18}$$

$$+ \overline{\langle \epsilon^2(N_p(E, \vec{r}, t)) \rangle} - \overline{\langle \epsilon(N_p(E, \vec{r}, t)) \rangle}^2 \tag{4.19}$$

We will now drop the explicit dependence on E and notationally replace $\epsilon(N_P)$ with N_P. This cleans up the the equation to:

$$\sigma^2_{N_P} = \overline{\langle N_p(\vec{r}, t)[1 - p_1(\vec{r})(1 + v_1(\vec{r}))] \rangle} + \overline{\left\langle N_p^2(\vec{r}, t) \right\rangle} - \overline{\langle N_p(\vec{r}, t) \rangle}^2 \tag{4.20}$$

This is further simplified by the introduction of the radial relative variance:

$$v_T(\langle N_p(\vec{r},t)\rangle) \equiv \frac{\left\langle N_p^2(\vec{r},t)\right\rangle - \langle N_p(\vec{r},t)\rangle^2}{\langle N_p(\vec{r},t)\rangle^2} \tag{4.21}$$

Substituting this definition into the previous equation yields:

$$\sigma^2_{N_P} = \overline{\langle N_p(\vec{r},t)[1-p_1(\vec{r})(1+v_1(\vec{r}))]\rangle} \tag{4.22}$$

$$+ \overline{(v_T(\langle N_p(\vec{r},t)\rangle)+1)\,\langle N_p(\vec{r},t)\rangle^2} - \overline{\langle N_p(\vec{r},t)\rangle}^2 \tag{4.23}$$

Next we make a few assumptions that allow us to make this result more manageable. The first one is that since p_1 and v_1 are both small, we treat them only to first order such that:

$$\langle N_p(\vec{r},t)[1-p_1(\vec{r})(1+v_1(\vec{r}))]\rangle = \langle N_p(\vec{r},t)\rangle \cdot \langle 1-p_1(\vec{r}(1+v_1(\vec{r}))\rangle \tag{4.24}$$

This allows us to write:

$$\sigma^2_{1_{N_P}} = \overline{\langle N_p(\vec{r},t)\rangle \cdot [1-\langle p_1(\vec{r})\rangle\,(1+v_1)]} \tag{4.25}$$

$$+ \overline{(v_T(\langle N_p(\vec{r},t)\rangle)+1)\,\langle N_p(\vec{r},t)\rangle^2} - \overline{\langle N_p(\vec{r},t)\rangle}^2 \tag{4.26}$$

where $v_1(t) \equiv \langle p_1(\vec{r})v_1(\vec{r})\rangle \,/\, \langle p_1(\vec{r})\rangle$. Using Eq. 4.13 and the new notational conventions and $N_p(t) \equiv \langle N_p(\vec{r},t)\rangle$, we have:

$$\sigma^2_{1_{N_P}} = \overline{N_p(t)\cdot[1-\frac{N_p(t)}{N_{live}(t)}(1+v_1)]} + \overline{[1+v_T(N_p(t))]\cdot N_p^2(t)} - \overline{N_p(t)}^2 \tag{4.27}$$

We point out that $N_p(t)$ is now the volume-averaged time-dependent expectation value of the N_p variable as seen in Eq. 4.8, rewriting with $f(t) \equiv N_{live}(t)/N_{fixed}$:

$$\sigma^2_{1_{N_P}} = \overline{N_{fixed} f(t) p_{1_{gc}}[1 - p_{1_{gc}}(1 + v_1)]} \tag{4.28}$$

$$+ \overline{[1 + v_T(N_p(t))](N_{fixed} f(t) p_{1_{gc}})^2} - \overline{N_p(t)}^2 \tag{4.29}$$

Next we assume from empirical observations that $v_T(N_p(t)) = v_T(\overline{N_p(t)})$. Including this as well as the notational change, $N_p = \overline{N_p(t)}$ we find:

$$\sigma^2_{2_{N_p}} = N_{fixed} p_{1_{gc}}[1 - p_{1_{gc}}(1 + v_1)]\overline{f(t)} + [1 + v_T(N_p)](N_{fixed} p_{1_{gc}})^2 \overline{f^2(t)} - N_p^2 \tag{4.30}$$

We define another relative variance $v_f = [\overline{f^2(t)} - \overline{f(t)}^2]/\overline{f(t)}^2$ to get:

$$\sigma^2_{2_{N_p}} = N_{fixed} p_{1_{gc}}[1 - p_{1_{gc}}(1 + v_1)]\overline{f(t)} \tag{4.31}$$

$$+ [1 + v_T(N_p)](N_{fixed} p_{1_{gc}})^2 \overline{f(t)}^2 (v_f + 1) - N_p^2 \tag{4.32}$$

Combining terms we get:

$$\sigma^2_{2_{N_p}} = N_p[1 - N_p/\overline{N_{live}}(1 + v_1)] + [v_f + v_T(N_p) + v_f v_T(N_p)]N_p^2 \tag{4.33}$$

The final assumption made to derive the final form is that $v_T(N_p) = v_T^0 N_p$ where v_T^0 is a constant. This assumption is based on MC modeling done in [30]. With this assumption we get:

$$\sigma^2_{3_{N_p}} = N_p[1 - Np/\overline{N_{live}}(1 + v_1)] + [v_f + v^0_T N_p + v_f v^0_T N_p]N^2_p \tag{4.34}$$

The final step is the addition of the component referred to as a "*pedestal*" term, σ^2_{ped}, that accounts for the presence of a variance that doesn't arise from scintillation events and is thus uncorrelated with energy. This yields the final form of:

$$\sigma^2_{3_{N_p}} = N_p[1 - Np/\overline{N_{live}}(1 + v_1)] + [v_f + v^0_T N_p + v_f v^0_T N_p]N^2_p + \sigma^2_{ped} \tag{4.35}$$

This is how we handle the response function for β events. Previous analyses have found that α events can be handled with the addition of a relative quenching factor that gives an effective energy in "β" units that is on the order of 10% that of the α event [39]. This is done empirically in the *spectral fitter* and is the only modification made for these event species.

4.3 Data Selection and Analysis Cuts

The data selection and cuts in this analysis largely follow those of the ^{7}Be analysis [6]. The data used here is from an 18 month timespan from January 1st 2012 through June 1st 2013 (see Table 4.1). This data is broken into 3 approximately equal length periods (9, 10, and 11) where we have used period 9 for the tuning of the analysis and produced the result on the combined statistics of periods 10 and 11. Periods 1 through 8 are referred to as Borexino Phase I and includes all the results that occurred before a scintillator purification campaign.

This analysis uses a subset of the cuts that were designed for the ^{7}Be analysis [6]. As the ^{7}Be had a higher threshold we've removed all of the cuts that would have an unknown effect on the shape of the ^{14}C pileup spectrum or on the Synthetic Spectrum (see Section 5.1). Below we list the cuts in the order they are applied and

Period	Dates	Run Range	Livetime[days]
9	Jan 01, 2012 - Jun 09, 2012	17407-18545	139.06
10	Jun 10, 2012 - Nov 17, 2012	18546-19359	146.28
11	Nov 18, 2012 - Jun 01, 2013	19360-20488	126.16

Table 4.1. Details on the subdivisions of the data used in this analysis

briefly describe the purpose of each. A detailed description of each cut can be found in Appendix A.

- Cut 1: Removes muons, cosmogenics, and post-muon noise.
- Cut 2: Removes triggers with no clusters or where the two reconstruction algorithms (Echidna and MOE) disagree on the total cluster number.
- Cut 3: Selects only inner detector triggers.
- Cut 4-6: Each removes a specific species of noise event.
- Cut 7: Removes triggers that have more than 2 clusters.
- Cut 8: Selects clusters that occur in the designed gate of the trigger window.
- Cut 9: Selects only events whose PMT hits are distributed reasonably isotropically.
- Cut 10: Selects events inside of our fiducial volume to remove external back grounds from the nylon vessels and vessel end-caps.

4.4 Spectral Fitter

One of the major endeavors for this analysis has been the upgrading of the Spectral Fitter tool used by the collaboration for spectral analysis, and specifically used for all of the fitting of energy spectra done in this analysis. We will omit most of the details

here as a large part of the upgrades were made to increase the user friendliness of the program.

The new energy response function (see Section 4.2) has been implemented in the Spectral Fitter. The new global free parameters in the analytical fit are now the fiducial volume averaged detector light yield Y_{det} and the parameters v_1, v_T^0, and σ_{ped}. The position of the ^{210}Po peak is also left free with respect to the β energy scale as it's high rate and distinct spectral shape allow the Spectral Fitter to determine these values more accurately than could be calculated from calibration data. In addition to these global parameters, the amplitudes of the solar *pp* neutrinos and the various background components are left free. The rate of other solar neutrino species have been constrained to their measured values in Borexino or to their predicted rate with the corresponding central value and error.

The fitter determines the free parameters via a binned maximum likelihood fit. We have chosen a likelihood fit, as opposed to chi-squared or other minimization methods, due to the possibility of low statistics in a number of our bins as well as the ability to include a penalty factor in the likelihood function due to parameters that we wish to constrain rather than fix.

In the case of a normal one-dimensional fit the Poissonian likelihood, L, of a hypothesis (the likelihood that the data fits a test spectrum with a given set of parameters $\vec{\theta}$) can be expressed as:

$$L(\vec{\theta}) = \prod_{i=1}^{n} \frac{\lambda_i(\vec{\theta})^{k_i} e^{-\lambda_i(\vec{\theta})}}{k_i!} \tag{4.36}$$

If we wish to apply a Gaussian constraint to a parameter, θ_1, we must add a term to the log-likelihood such that:

$$-2 \cdot ln(L(\vec{\theta})) = -2 \cdot \sum_{i=1}^{n} ln(\frac{\lambda_i(\vec{\theta})^{k_i} e^{-\lambda_i(\vec{\theta})}}{k_i!}) + \frac{(\theta_1 - \theta_1^{constraint})^2}{\sigma_{\theta_1}^2} \tag{4.37}$$

where $\theta_1^{constraint}$ is the mean and $\sigma_{\theta_1}^2$ is the variance of the constrained parameter. This method is used when we want to include information, the mean and standard deviation, from a previous measurement in our fit.

CHAPTER 5

^{14}C PILEUP ANALYSIS

5.1 Synthetic Spectra

The Synthetic Spectra are one of the tools that we have developed to address the pileup of ^{14}C in our detector [40]. It is a simulation method that builds overlapped events using trigger data overlapped with noise events from the detector. It uses actual events from our data and then superimposes additional PMT hits from a real trigger by randomly sampling our detector background. In these time periods there will be ^{14}C events that have overlapped, simply by chance, on top of our original data event, thus creating realistic pileup. We search for these instances and select them to form our Synthetic Spectra. These spectra are then used as an input in the Spectral Fitter to account for this event population in our data.

5.1.1 Procedure

This section is a technical discussion of the procedure used to produce the Synthetic Spectra. In order to do this, we must first outline the data flow structure of Borexino. Data for each trigger begins in a state referred to as "raw data" which is processed by the low-level reconstruction code (Echidna). This low-level data consists of basic information from the trigger like which PMTs were hit and at what time (*decoded hits*). This information is then used in the high-level reconstruction, Echidna or Mach4 Over Echidna(MOE), that includes clustering, and energy/position reconstruction (see Section 4.1). Our procedure hijacks the data flow at the low level to create new sets of synthesized events for processing by the high-level MOE analyses.

For each trigger in the low-level files we take all of the decoded hits that occur in a fixed 3μs window at the end of the trigger gate and overlap (copy) them on top of the first 3μs of the trigger gate. This is accomplished by creating a copy of each hit in the window and shifting the timing of that copy back by the appropriate amount. The start of the trigger now contains the decoded hits from the event that caused the trigger as well as any hits that were copied from the end of the trigger window. This process is repeated for every trigger in each run used for this analysis.

Figure 5.1 and Figure 5.2 show the distribution of decoded hits in a single trigger before and after it has passed through the Synthetic Pileup process. This particular trigger has a muon at the end of it and has many more hits than a typical trigger included in the analysis but it was selected for the ease with which the copying process can be seen.

After each trigger has been processed we have a pair of files for each run. The original/base file, which is the same run file that is used to construct the final energy spectrum used for analysis, and the synthetic file which has extra hits overlapped in every trigger. We then compare the energy (npmts_dt1) of each of the original clusters with the energy of its synthetic partner and classify the synthetic event by the number of extra hits that were overlapped in the process. In order to correcly simulate detector behavior we need to remove instances where the added event is overlapped before the event that triggered the detector. We do this by only selecting synthetic clusters that start at the same time as the cluster in the base trigger.

Events are saved if they have increased in energy through this process. They are then passed through all of the cuts used in the *pp* analysis (see Section 4.3). From these events we then produce several spectra that differ in the minimum change in energy we require between the base and synthetic event (e_min). This is done to eliminate events that changed in energy as a result of additional dark noise hits from PMT fluctuations getting added instead of physical events inside the detector.

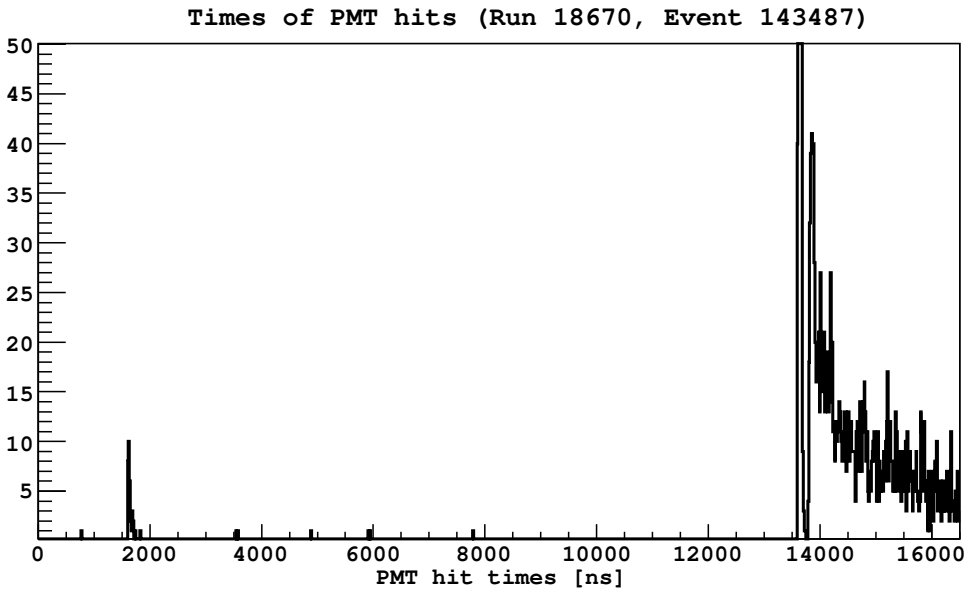

Figure 5.1. A raw trigger before any hits have been copied. The event that caused the trigger can be seen near 2000 ns. At the end of the trigger gate is a large number of hits caused by a muon that happened to coincide with this other event.

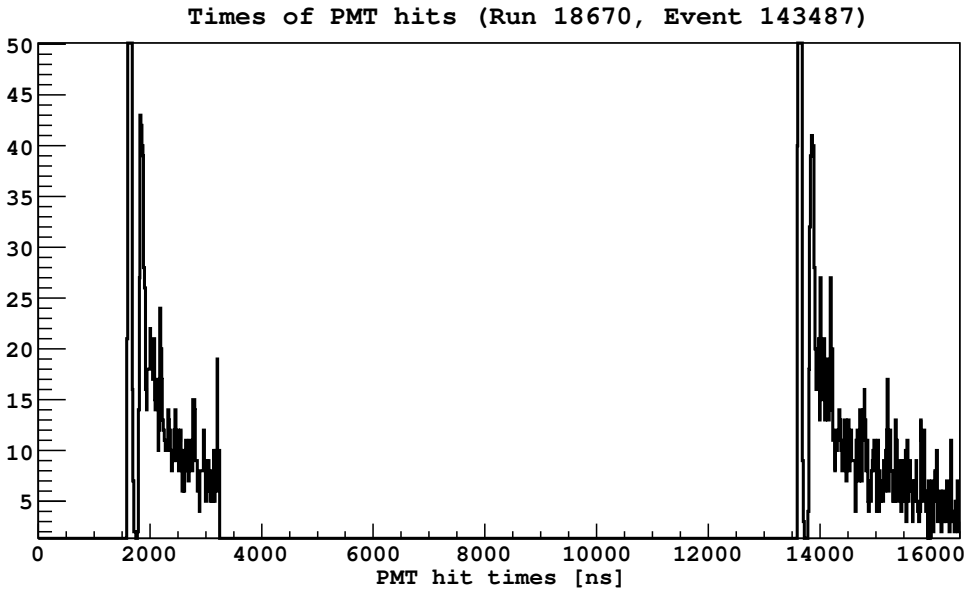

Figure 5.2. The same trigger from Figure 5.1 after hits have been copied from 3μs at the end of the trigger.

Synthetic Set	Trigger Window for Decoded Hit Copying(ns)
01	12000-15000
02	13000-16000
03	12500-15500
04	11000-14000

Table 5.1. The trigger time regions at the end of the trigger gate from where hits are copied for each synthetic set.

In order to increase the statistics of the Synthetic Spectra, the entire process is repeated four times using the same method but the time window used from the end of the trigger is shifted by at least 500ns from each of the other sets(see Table 5.1). The four resulting spectrum for each value of minimum energy are averaged together to create a single Synthetic Spectrum with higher precision.

Each Synthetic Spectrum includes the spectral contributions due to the dark-rate of the detector for events greater than or equal to the value of e_min used to construct it. Therefore, it's necessary to convolve (see Section 5.2) the analytical functions in the fit with the detector's dark noise spectrum (Figure 5.3) only up to the minimum energy used to generate the chosen Synthetic Spectrum.

5.1.2 Results

To validate the results of this method we fit the spectrum that is generated with an e_min = 10 with ^{14}C-pileup analytical function in the fitter (see Figure 5.4). This value of e_min is high enough to guarantee that the synthetic pileup events are pure ^{14}C with ^{14}C (or other "high" energy events) and not with the buffer and noise events that dominate lower in the spectrum(see Figure 5.3).

We find that the analytical shape for ^{14}C pileup fits this spectrum extremely well. We find an equivalent rate of 160 ± 14 cpd/100t. If we compare this with a naive description of pileup in which all pileup consists of a ^{14}C event in the fiducial volume (75.5 t) that has had a ^{14}C event from anywhere in the inner vessel (278 t) and that

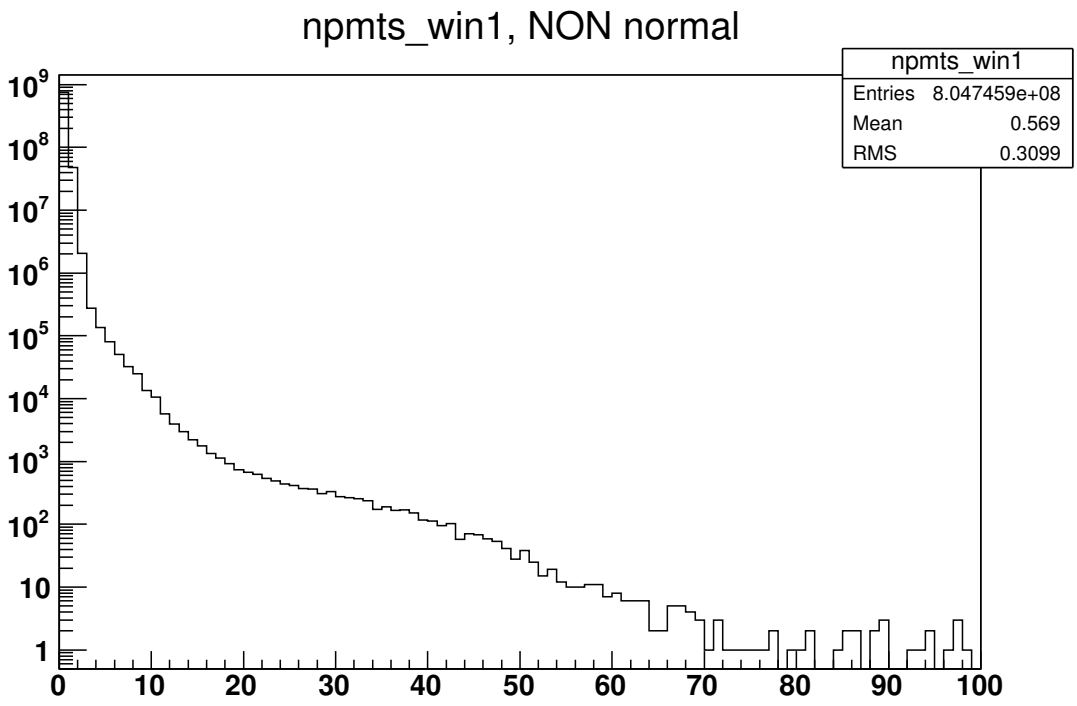

Figure 5.3. Spectrum of the dark noise in Borexino made from random triggers split into windows that are 230ns long.

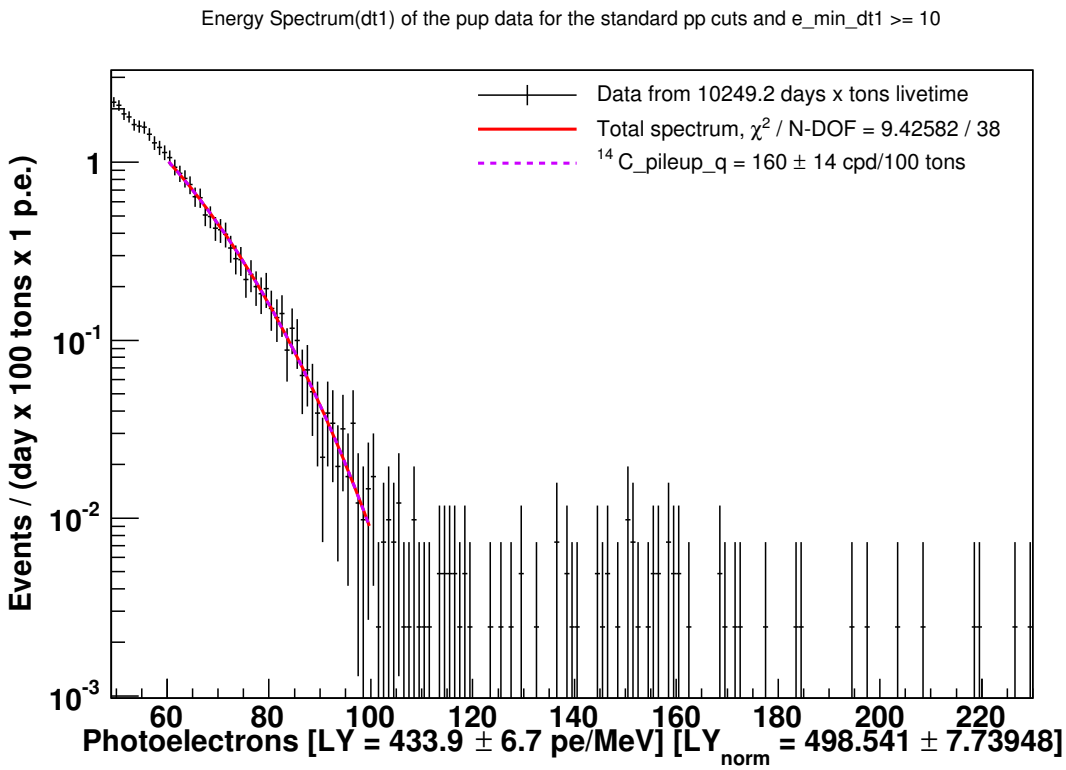

Figure 5.4. Fit of the Synthetic Spectrum generated with e_min = 10 from period 9 with the analytical ^{14}C Pileup function.

we have $\sim$ 43 Bq/100t of ^{14}C in the scintillator. We can then estimate 102 cpd/100t of pileup which is quite consistent with the result we found given that the assumptions are an under-estimate.

5.1.3 Systematic Effects

There are a number of known systematics associated with this method for the generation of ^{14}C pileup events compared to the true effect in the detector:

- Base events include dark noise already: <1%
- Base events aren't pure ^{14}C: <0.001% error
- Base events are the same in all 4 sets: 0.01%

- Slightly different analysis cuts due to having access to only MOE variables: $<$ 0.01%

The first systematic effect is due to the fact that the dark rate of the PMTs exists behind the base event as well as any additional event piled up with it. This means that we have effectively twice the dark rate of PMTs in our synthetic spectrum. Fortunately the dark rate in Borexino is such that the probability of having ≥ 1 hit added to an event is less than 10%. This makes the fraction of synthetic events that have a dark rate contribution in both events used to construct the synthetic event below 1%.

The second systematic effect accounts for the presence of other event types in the data. However, the rate of these events are so many orders of magnitude below that of ^{14}C that the effect is completely negligible. The next effect is due to the fact that we always start with the same data set before overlap with the different time windows. The fraction of these base events that end up in the final Synthetic Spectrum that is so small that the probability of the same event ending up in more than one final set is extremely small.

The final effect is due to the technical limitations of the method. The synthetic data contains only information about variables produced by the MOE high-level analysis whereas the data used to produce the final energy spectrum for fitting uses both MOE and Echidna high-level variables (see Section 4.1). This effect is estimated by comparing an energy spectrum produced using the version of the cuts adapted for the synthetic files to the energy spectrum produced by the analysis cuts. The final spectrum are extremely similar and the resulting change is small.

5.2 Convolution Method

A second method for handling the pileup involves ignoring ^{14}C pileup as an independent species but convolving each of the analytic spectra with the full range of the

dark noise spectrum. The dark noise spectrum is generated by breaking the random triggers, that occur once every two seconds, into many windows of the desired length (230 ns for dt1 and 400 ns for dt2). Figure 5.3 shows this spectrum for the sum of periods 10 and 11. The other method this analysis uses to address ^{14}C pileup is what is referred to as the Convolution Method. This method takes the process of convolving the analytical functions in the fitter with the dark noise in the detector to its extreme. Rather than including any species for pileup in the fitter, the sum of all the other species is instead convolved with the dark noise spectrum all the way through a value of 100. This method has many known disadvantages, the largest being that it assumes that the pileup hits have no impact on the event reconstruction beyond increasing its energy. This is equivalent to stating that all of the pileup that ends up in our data is the result of an event inside our fiducial volume piled-up with a second event taken from anywhere inside the detector. However, this method provides a very important independent check of the Synthetic Method since the resulting fit doesn't depend on either the rate or the shape of the Synthetic Spectra.

CHAPTER 6

FIRST DIRECT DETECTION OF *PP* SOLAR NEUTRINOS

Reported in this chapter is the first measurement of the *pp* solar neutrino interaction rate in Borexino. We find the rate of *pp* ν-electron elastic scattering interactions to be $155 \pm 16(stat) \pm 13(sys)$ counts per day per 100 tonnes (cpd/100 t). This result comes from fitting the measured energy spectrum of events in the window of 60 - 230 npmts_dt1 ($\sim$165 - 590 keV) from 356 days of Borexino data from June 10th, 2012 to June 1st, 2013 with the theoretical spectra of the signal and background components using the Spectral Fitter tool described in Section 4.4.

6.1 Fit Results

We take the central value and statistical error from our baseline fit (see Figure 6.1). If we include the systematic uncertainties, all summarized in Table 6.1 and Table 6.2, and we find our final result for the measured *pp* interaction rate to be $155 \pm 16(stat) \pm 13(sys)$ counts/day/100 t. The combined uncertainty on the central value is 13.3%. The estimation of systematic uncertainties hinges deeply on the level of understanding of the detector. Significant efforts have been made to be as accurate as possible when evaluating the sources of systematics. In agreement with our systematic uncertainty, we note that none of the various fits we have tabulated here nor many others that have been produced via numerous iterations of the fitting procedure have produced a result that falls outside of the 3σ(39 cpd/100 t) systematic range of the central value reported here.

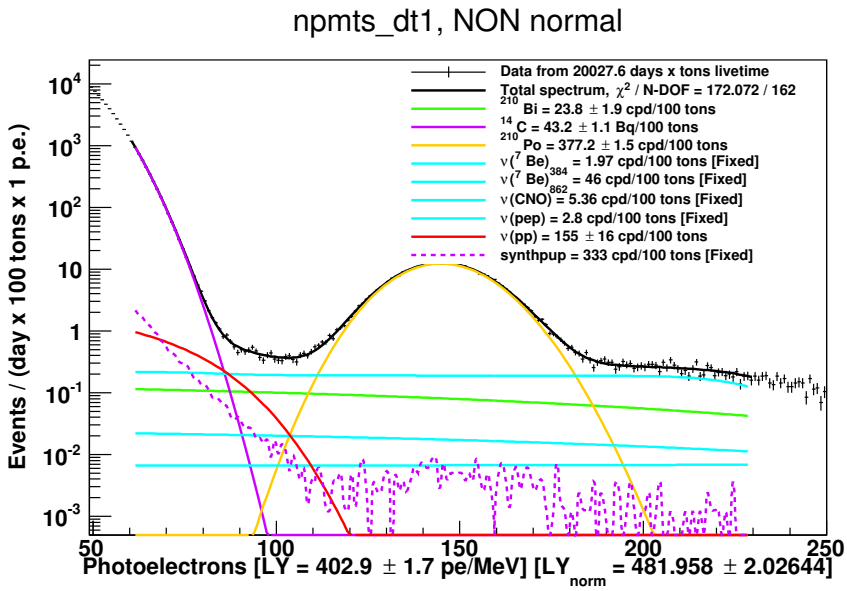

Figure 6.1. Fit of the Borexino Energy Spectra with the result of the *pp* analysis.

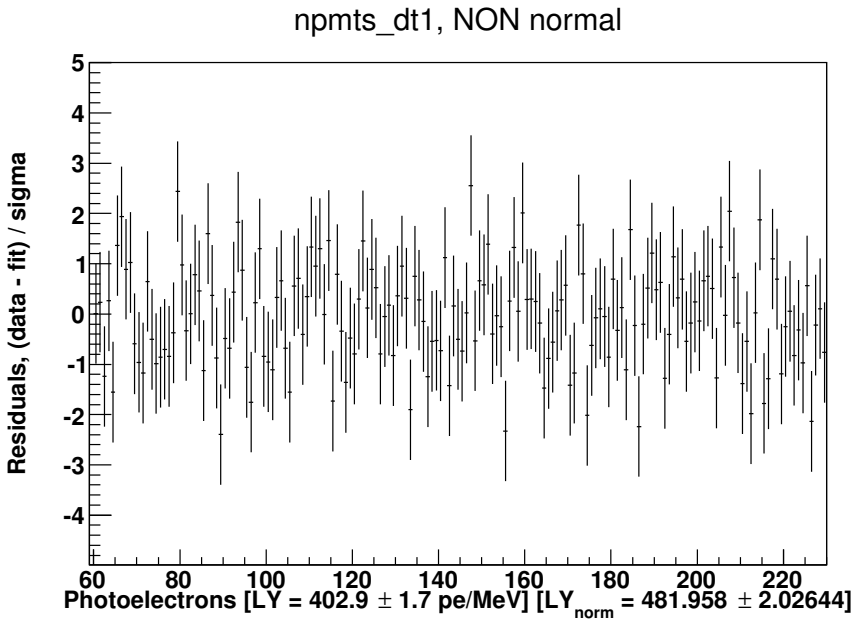

Figure 6.2. Residuals of the fit of the Borexino Energy Spectra with the result of the *pp* analysis in Figure 6.1.

Period[F]	Range[F] (bins)	q[F]	Pileup[F]	pp Rate[R] (cpd/100t)	L.Y. [R] (p.e./MeV)	Chi^2/DoF	P-Value
10+11	**60-230**	**dt1**	**synth_5**	**155±16**	**402.9±1.7**	**172.1/162**	**0.279**
10+11	60-230	dt1	DN_conv	154 ± 17	402.6 ± 2.5	171.4/162	0.291
10+11	60-230	dt1	synth_10	155 ± 16	402.9 ± 2.7	171.5/162	0.290
10+11	60-230	dt1	synth_5[10%P]	155 ± 17	402.9 ± 2.6	181.79/161	0.125
10+11	60-230	dt2	synth_5	167 ± 16	408.2 ± 2.3	166.2/162	0.395
10+11	60-230	dt2	synth_10	168 ± 16	408.2 ± 2.4	166.1/162	0.396
10+11	60-230	dt2	full_DN	148 ± 15	408.11 ± 0.38	166.8/162	0.383
10+11	55-225	dt1	synth_5	154 ± 16	403.7 ± 1	167.2/162	0.373
10+11	63-233	dt1	synth_5	156 ± 17	401.4 ± 3.6	170.3/162	0.311
10	60-230	dt1	synth_5	146 ± 22	408 ± 3.2	192.2/162	0.053
11	60-230	dt1	synth_5	161 ± 20	398.9 ± 3.5	173.2/162	0.258
Fit in reduced a FV with r < 2.5 instead of r < 3.021 (Used connonical FV geometrical correction factor)							
10+11	60-230	dt1	synth_5	149 ± 20	403.9 ± 3.5	180.637/162	0.150
Null Hypothesis (no pp in the fit)							
10+11	60-230	dt1	DN_conv		396.9 ± 1.4	256.5/163	4.03E-6
10+11	60-230	dt1	synth_5[10%P]		418.0 ± 0.18	410.4/162	1.63E-23

Table 6.1. Table of the fit results for different fit conditions with the baseline fit is highlighted in bold. Columns labeled [F] are fixed prior to the launching of the fit and columns marked with [R] are values returned by the fit. Parameters marked with [%P] have been constrained in the likelihood fit by a gaussian with the given percentage as the standard deviation. This table includes the data period (Period), the fit range (Range), the energy estimator used (q = npmts_dt1/2), the method used to handle ^{14}C pileup(Pileup), the *pp* interaction rate in Borexino (*pp* Rate), the Chi^2 per degree of freedom, and the p-value of the result.

Source	Value[%]
Trigger efficiency and stability	< 0.1
Live-time	< 1
Scintillator density	< 0.1
Fiducial Mass	1
Pileup Method	0.7
Fit Range	0.7
Energy Variable	8.3
Total Systematic Error	± 8.4

Table 6.2. Systematic uncertainties in the central value of the *pp* solar neutrino interaction rate. The total rate is calculated by combining them under the assumption there are no correlations between the sources.

6.2 Systematic Errors

Table 6.2 summarizes all of the systematic effects considered in this analysis. The total systematic error is calculated as the individual errors combined in quadrature. The following subsections detail how these effects have been estimated.

6.2.1 Fit Range

The method for the estimation of this effect can be seen in Table 6.1. Two alternate fit ranges with equal degrees of freedom have been selected, 55-225 and 63-233. There is an upper limit on the selection of the lower limit of the fit range placed due to the ability of the fitter to accurately measure the ^{14}C rate based on the reduced statistics present in the tail of the spectrum.

6.2.2 Energy Variable

The systematic effect associated with choosing either npmts_dt1 or npmts_dt2 as our energy variable depends on the way ^{14}C pileup is handled. For the synthetic method we find a systematic effect of +8% and for the full convolution method we find -5%. Since these methods agree very well for npmts_dt1 we choose to associate the entirety of this effect as a $\pm 8\%$ systematic effect on the selection of energy variable.

Period[F]	Range[F] (bins)	q[F]	Pileup[F]	^{14}C Rate[R] (Bq/100t)	^{210}Bi [R] (cpd/100t)	^{210}Po (cpd/100t)
10+11	**60-230**	**dt1**	**synth_5**	**43.2±1.1**	**23.8±1.9**	377.2 ± 1.5
10+11	60-230	dt1	DN_conv	43.5 ± 1.7	24 ± 2	377.3 ± 1.5
10+11	60-230	dt1	synth_10	43.3 ± 1.8	24.2 ± 2	377.3 ± 1.5
10+11	60-230	dt1	synth_5[10%P]	43.2 ± 1.7	23.8 ± 2	377.2 ± 1.5
10+11	60-230	dt2	synth_5	42.1 ± 1.5	23.3 ± 1.9	377.3 ± 1.5
10+11	60-230	dt2	synth_10	42.2 ± 1.5	23.7 ± 1.5	377 ± 1.5
10+11	60-230	dt2	full_DN	42.27 ± 0.28	23.2 ± 1.8	377.7 ± 1.5
10+11	55-225	dt1	synth_5	42.69 ± 0.54	24.1 ± 2	377.1 ± 1.5
10+11	63-233	dt1	synth_5	44.6 ± 2.7	24.2 ± 2	377 ± 1.5
10	60-230	dt1	synth_5	44.2 ± 2.1	24.6 ± 2.6	483.8 ± 2.3
11	60-230	dt1	synth_5	40.9 ± 2.5	22.9 ± 2.8	252.8 ± 1.9
Fit in reduced a FV with r < 2.5 instead of r < 3.021 (connonical FV gc factor)						
10+11	60-230	dt1	synth_5	41.7 ± 2.3	24.3 ± 2.5	381 ± 1.9
Null Hypothesis (no pp in the fit)						
10+11	60-230	dt1	DN_conv	46.9 ± 1	32.5 ± 1.6	375.4 ± 1.5
10+11	60-230	dt1	synth_5[10%P]	33.89 ± 0.18	35.6 ± 1.2	374.7 ± 1.1

Table 6.3. Table of the fit results for the background species for different fit conditions with the baseline fit highlighted in bold. Columns labeled [F] are fixed prior to the launching of the fit and columns marked with [R] are values returned by the fit. Parameters marked with [%P] have been constrained in the likelihood fit by a gaussian with the given percentage as the standard deviation. This table includes the data period (Period), the fit range (Range), the energy estimator used (q = npmts_dt1/2), the method used to handle ^{14}C pileup(Pileup), the ^{14}C, ^{210}Bi, and ^{210}Po background rates.

The large contribution of this effect resulted in a lot of work to try to reduce its effect. The only current explanation is that the typical length of a cluster used for position reconstruction (see Section 4.1) lies between the fixed cluster lengths of 230ns and 400ns used to calculate the npmts_dt1 and npmts_dt2 energy estimators respectively.

6.3 Background Stability

This section briefly examines the stability of the background rates returned by the fit for the various systematic tests (see Table 6.3).

6.3.1 ^{14}C Rate

The ^{14}C rate is extremely stable (with the exception of the null hypothesis) around the measured value of 43.2$\pm$1.1 Bq/100t. All of the results for the selected fit options are consistent within 1σ of each other. This rate in 100 tonnes is equivalent to an isotopic abundance of 2.75×10^{-18} ^{14}C/^{12}C in the scintillator.

6.3.2 ^{210}Bi and ^{210}Po Rates

The most notable difference in Table 6.3 the difference in the ^{210}Po rate between period 10 and period 11. This is to be expected as the half life of ^{210}Po is 138 days and each period is about 6 months long (see Table 4.1). The fact that the change in this rate isn't completely consistent with a 138 day half life (even including a source term from the measured ^{210}Bi) is one of the main indicators of convection currents in the scintillator circulating particulate matter around the inner vessel.

The rate of ^{210}Bi remains stable within 1σ over all of the systematic checks. The relatively short half life of 5 days for ^{210}Bi with respect to 23.2 years for its parent nucleus, ^{210}Pb, is expected to place it in secular equilibrium inside the scintillator. This is consistent with our findings of a ^{210}Bi rate of 24.6 ± 2.6 and 22.9 ± 2.8 for periods 10 and 11 respectively.

6.4 Interpretation of Results

The measured result of this analysis is the rate of interaction of the *pp* neutrinos via neutrino-electron elastic scattering. This rate can be converted into the *pp* neutrino flux by including the cross section for interaction, solar neutrino oscillations, and the number of electrons in the target:

$$R = (\phi_{\nu_e}\sigma_{\nu_e} + \phi_{\nu_{\mu,\tau}}\sigma_{\nu_{\mu,\tau}})n \tag{6.1}$$

where R is the measured interaction rate, ϕ_{ν_x} is the electron neutrino flux or the combined muon and tau neutrino flux, σ_x is the total electron scattering cross section for the corresponding neutrino flavor, and n is the number of electrons in the target. We are not able to directly determine the total neutrino flux due to the dependence on the scattering cross sections.

For *pp* neutrinos $\sigma_{\nu_{\mu,\tau}} \simeq 3.3\times10^{-46}cm^2$, $\sigma_{\nu_e} \simeq 11.6\times10^{-46}cm^2$ [37], $R = (155\pm20)$ cpd/100 t, where we've combined the statistical and systematic errors in quadrature, and $n = (3.307 \pm 0.003) \times 10^{31}$ electrons/100 t in the scintillator target.

In the case of no neutrino oscillations, where all neutrino-electron scattering is assumed to be purely from ν_e, and the total *pp* neutrino flux is taken from the high metallicity Standard Solar Model(GS98), the predicted interaction rate from Eq. 6.1 is 198 ± 1 cpd/100 tons. We are able to exclude the case of no neutrino oscillations at the 2σ confidence level with our result.

In the next two subsections we alternately assume the SSM predictions or the LMA-MSW oscillation solution to calculate the electron neutrino survivability and the total *pp* solar neutrino flux respectively implied by our result.

6.4.1 Calculation of P_{ee} Based on Solar Predictions

If we assume that the total flux is constrained to $5.98(1\pm0.006)\times10^{10}cm^{-2}sec^{-1}$, the value coming from the SSM(GS98), and a single effective value for P_{ee} across the full *pp* spectrum. We then obtain $P_{ee} = 0.695 \pm 0.141(1\sigma)$ where the uncertainty is dominated by our measurement. This value is high but still consistent with the predicted value of $P_{ee} \simeq 0.546$ for neutrinos at 0.1MeV and $P_{ee} \simeq 0.565$ for neutrinos in a vacuum.

6.4.2 Calculation of *pp* ν Flux Assuming LMA-MSW

If take the LMA-MSW solution for the neutrino oscillations to calculate $P_{ee} = 0.542 \pm 0.016$, we then find $\phi_{tot}(LMA) = (6.96 \pm 0.91) \times 10^{10}\text{cm}^{-2}\text{sec}^{-1}$ for the

total solar pp neutrino flux. Comparing this value to $\phi(GS98) = (5.98 \pm 0.04) \times 10^{10}\text{cm}^{-2}\text{sec}^{-1}$ and $\phi(AGSS09) = (6.03 \pm 0.04) \times 10^{10}\text{cm}^{-2}\text{sec}^{-1}$ we see that while the results are high at the level of just over 1σ we are not able to distinguish between the high(GS98) and low(AGSS09) metallicity solutions due to the dominance of the uncertainty in our measurement.

6.5 Other Backgrounds

In the measurement of the ^{7}Be neutrinos one of the important backgrounds was that of ^{85}Kr. There are two reasons why we've chosen not to include this in our final analysis. The first is that an independent search for ^{85}Kr activity by looking for $^{85}\text{Kr}\rightarrow^{85m}\text{Rb}$ delayed coincidences has shown that the rate has been substantially reduced by the purification campaigns in the scintillator. Secondly, as a check we've performed a fit with ^{85}Kr and left it free. We have found a rate of 5.4 ± 5.5 cpd/100 t for ^{85}Kr and the results for the pp neutrinos remain consistent. However, there is a decrease in the central value for the ^{210}Bi background and an increase in it's uncertainty as a result of the spectral contribution assigned to ^{85}Kr.

Another background of possible concern is the β emitter, ^{87}Rb. It has a half-life of 4.8×10^{10} years, 28% isotopic abundance, and a Q-value of 283.3 keV. Rubidium is an alkali metal that is chemically close to potassium but typically 2000-4000 times less abundant in the crust. We assume then that the processes involved in manufacturing and purification of the scintialltor have treated these two elements the same. Combining this with the measured ^{40}K (half-life of $.48 \times 10^{10}$ years and 0.0117% isotopic abundance) activity in the fiducial volume of < 0.4 cpd/100 t at the 95% confidence level [32], the ^{87}Rb activity can be constrained at less than 0.1 cpd/100 t, which is negeligeble for this analysis.

6.6 Outlook

This work presents the first direct detection of the low-energy *pp* neutrinos produced by the primary proton-proton fusion reaction in the Sun's core. This process is the fundamental process responsible for the energy production in the Sun and is responsible for the vast majority of solar neutrinos. This achievement by Borexino is a milestone in particle astrophysics and demonstrates how far the experiment has extended past its design goals. This measurement was possible due to the unprecedentedly low levels of radioactive backgrounds reached inside the detector. The experimental uncertainty does not allow us to distinguish between the details of the various Standard Solar Models but it does allow us to confirm our understanding of the Sun and shows that the processes that drive it have remained relatively consistent over the past $\sim 10^6$ years.

The next logical question is the feasibility of a precision measurement using the same techniques with more data or new analysis methods. The current limits on the statistical and systematic uncertainties are dominated by the effects assosiated with the ^{14}C background and its pileup. One of the proposed methods for handling this, counterintuitively, involves the injection of extra ^{14}C into the scintillator in the form of dissolved CO_2 with a very high isotopic ratio of ^{14}C. A measurable increase in the ^{14}C rate would cause a corresponding increase in the pileup rate and the ratio of this rate could be used to constrain a multidimension fit between the two detector cases where all other components would be the same. This method would be extremely invasive to the detector and initial studies have had mixed success in the stripping of the added gas back out of the scintillator. Less invasive options involve finding better analysis methods or clustering algorithms for identifying and removing the pileup events in the detector. Unfortunately the energy of the events in question is low enough that there is not a lot of discriminatory power available to new methods.

However, this still remains the best avenue for a precision measurement of low-energy solar neutrinos with a liquid scintillator based detector.

APPENDIX

ANALYSIS CUTS

The cuts are all made in $bxfilter/local/pp\_data.cc$.

1. Muons, Cosmogenics, and Post-Muon Noise

   if (muon_internal) tag and drop event

   if ($\Delta t_\mu < 300ms$)

   if (muon_internal and not muon_special_d1) restart 300ms window and drop event

   else drop event

2. Zero cluster events and Clustering consistency

   if ($n\_cl\_echidna = 0 || n\_cl\_m4 = 0 || n\_cl\_echidna \neq n\_cl\_m4$)

   drop event

3. Keep only trigger type = 1

   if ($trg\_type \neq 1 || btb\_inputs \neq 0$)

   drop event

4. Q/Qrec

   if !($0.6 < \frac{charge}{qrec} < 1.6$)

   drop event

   qrec = $-2000ln(1 - \frac{npmts\_short}{2000}) \cdot (1 + 0.11ln(1 - \frac{npmts\_short}{2000}))$

5. M4 strange events

   if $(\frac{charge\_noavg\_m4}{charge\_m4} < 0.5 \cdot \frac{good\_charge\_channels\_m4}{n\_live\_pmts\_m4})$

   drop event

6. Drop crate Noise

   if $(m4\_laben\_hitdist\_1\_crate\_frac > 0.75)$

   drop event

7. Drop Events with > 2 clusters

   if $(n\_clusters\_echidna > 2)$

   drop event

8. Start time of cluster

   if $!(500ns < cluster\_start\_time < 1990ns)$

   drop event

9. Geometrical uniformity

   if $(beta\_recon > 0.02657 + e^{(-1.306-0.01728 \cdot charge\_m4)} + e^{(-3.199-0.001738 \cdot charge\_m4)})$

   drop event

10. FV cut

    if $(r\_lngs > 3.021 || abs(z\_lngs) > 1.67)$

    drop event

BIBLIOGRAPHY

[1] **Particle Data Group** Collaboration, J. Beringer, K. Nakamura, *et al.*, "Review of particle physics," *Phys. Rev. D* **86** (Jul, 2012) 010001. http://link.aps.org/doi/10.1103/PhysRevD.86.010001.

[2] A. M. Serenelli, W. Haxton, and C. Pena-Garay, "Solar models with accretion. i. application to the solar abundance problem," *Astrophys.J.* **743** (2011) 24, arXiv:1104.1639.

[3] **Borexino** Collaboration, G. Bellini *et al.*, "Measurement of the solar 8B neutrino rate with a liquid scintillator target and 3 MeV energy threshold in the Borexino detector," *Phys.Rev.* **D82** (2010) 033006, arXiv:0808.2868 [astro-ph].

[4] **KamLAND** Collaboration, S. Abe *et al.*, "Production of Radioactive Isotopes through Cosmic Muon Spallation in KamLAND," *Phys.Rev.* **C81** (2010) 025807, arXiv:0907.0066 [hep-ex].

[5] E. G. Adelberger, A. Garcia, Robertson, *et al.*, "Solar fusion cross sections. ii. the *pp* chain and cno cycles," *Rev. Mod. Phys.* **83** (Apr, 2011) 195–245. http://link.aps.org/doi/10.1103/RevModPhys.83.195.

[6] **Borexino** Collaboration, G. Bellini *et al.*, "Precision measurement of the ^{7}be solar neutrino interaction rate in borexino," *Phys. Rev. Lett.* **107** (Sep, 2011) 141302. http://link.aps.org/doi/10.1103/PhysRevLett.107.141302.

[7] V. Barger, D. Marfatia, and K. Whisnant, "Testing the {LMA} solution with solar neutrinos independently of solar models," *Physics Letters B* **617** no. 12, (2005) 78 – 86. http://www.sciencedirect.com/science/article/pii/S0370269305006027.

[8] F. Reines and C. L. Cowan, "Detection of the free neutrino," *Phys. Rev.* **92** (Nov, 1953) 830–831. http://link.aps.org/doi/10.1103/PhysRev.92.830.

[9] L. Brown, "The idea of the neutrino," *Physics Today* **31** (Sep, 1978) 23. http://dx.doi.org/10.1063/1.2995181.

[10] **Planck** Collaboration, P. Ade *et al.*, "Planck 2013 results. XVI. Cosmological parameters," arXiv:1303.5076 [astro-ph.CO].

[11] H. A. Bethe, "Energy production in stars," *Phys. Rev.* **55** (Jan, 1939) 103–103. http://link.aps.org/doi/10.1103/PhysRev.55.103.

[12] B. J., *Neutrino Astrophysics.* Cambridge University Press, 1989. http://www.sns.ias.edu/~jnb/.

[13] P. de Holanda, W. Liao, and A. Y. Smirnov, "Toward precision measurements in solar neutrinos," *Nucl.Phys.* **B702** (2004) 307–332, arXiv:hep-ph/0404042 [hep-ph].

[14] J. N. Bahcall, "The luminosity constraint on solar neutrino fluxes," *Phys. Rev. C* **65** (Jan, 2002) 025801. http://link.aps.org/doi/10.1103/PhysRevC.65.025801.

[15] L. Wolfenstein, "Neutrino oscillations in matter," *Phys. Rev. D* **17** (1978) 2369–2374.

[16] S. P. Mikheyev and A. Y. Smirnov, "Resonance enhancement of oscillations in matter and solar neutrino spectroscopy," *Yadernaya Fizika* **42** (1985) 1441–1448.

[17] R. Davis, D. S. Harmer, and K. C. Hoffman, "Search for neutrinos from the sun," *Phys. Rev. Lett.* **20** (May, 1968) 1205–1209. http://link.aps.org/doi/10.1103/PhysRevLett.20.1205.

[18] **GALLEX** Collaboration, W. Hampel *et al.*, "GALLEX solar neutrino observations: Results for GALLEX IV," *Phys.Lett.* **B447** (1999) 127–133.

[19] **GNO** Collaboration, M. Altmann *et al.*, "Complete results for five years of GNO solar neutrino observations," *Phys.Lett.* **B616** (2005) 174–190, arXiv:hep-ex/0504037 [hep-ex].

[20] **SAGE** Collaboration, J. Abdurashitov *et al.*, "Measurement of the solar neutrino capture rate with gallium metal. III: Results for the 2002–2007 data-taking period," *Phys.Rev.* **C80** (2009) 015807, arXiv:0901.2200 [nucl-ex].

[21] C. Pena-Garay and A. Serenelli, "Solar neutrinos and the solar composition problem," arXiv:0811.2424 [astro-ph].

[22] Y. Fukuda, T. Hayakawa, *et al.*, "Solar neutrino data covering solar cycle 22," *Phys. Rev. Lett.* **77** (Aug, 1996) 1683–1686. http://link.aps.org/doi/10.1103/PhysRevLett.77.1683.

[23] **Super-Kamiokande** Collaboration, K. Abe *et al.*, "Solar neutrino results in super-kamiokande-iii," *Phys. Rev. D* **83** (Mar, 2011) 052010. http://link.aps.org/doi/10.1103/PhysRevD.83.052010.

[24] **SNO** Collaboration, B. Aharmim *et al.*, "Combined Analysis of all Three Phases of Solar Neutrino Data from the Sudbury Neutrino Observatory," *Phys.Rev.* **C88** (2013) 025501, arXiv:1109.0763 [nucl-ex].

[25] G. A. et. al., "The borexino detector at the laboratori nazionali del gran sasso," *Nuclear Instruments and Methods in Physics Research Section A: Accelerators, Spectrometers, Detectors and Associated Equipment* **600** no. 3, (2009) 568 – 593. http://www.sciencedirect.com/science/article/pii/S016890020801601X.

[26] **Borexino Collaboration** Collaboration, G. Alimonti *et al.*, "Science and technology of BOREXINO: A Real time detector for low-energy solar neutrinos," *Astropart.Phys.* **16** (2002) 205–234, arXiv:hep-ex/0012030 [hep-ex].

[27] J. Benziger *et al.*, "A scintillator purification system for the borexino solar neutrino detector," *Nuclear Instruments and Methods in Physics Research Section A: Accelerators, Spectrometers, Detectors and Associated Equipment* **587** no. 23, (2008) 277 – 291. http://www.sciencedirect.com/science/article/pii/S016890020800003X.

[28] G. Alimonti *et al.*, "The liquid handling systems for the borexino solar neutrino detector," *Nuclear Instruments and Methods in Physics Research Section A: Accelerators, Spectrometers, Detectors and Associated Equipment* **609** no. 1, (2009) 58 – 78. http://www.sciencedirect.com/science/article/pii/S0168900209014247.

[29] M. Chen, F. Elisei, *et al.*, "Quenching of undesired fluorescence in a liquid scintillator particle detector," *Nuclear Instruments and Methods in Physics Research Section A: Accelerators, Spectrometers, Detectors and Associated Equipment* **420** no. 12, (1999) 189 – 201. http://www.sciencedirect.com/science/article/pii/S0168900298011334.

[30] **Borexino** Collaboration, G. Bellini *et al.*, "Final results of Borexino Phase-I on low energy solar neutrino spectroscopy," arXiv:1308.0443 [hep-ex].

[31] C. Arpesella, G. Bellini, *et al.*, "First real time detection of 7be solar neutrinos by borexino," *Physics Letters B* **658** no. 4, (2008) 101 – 108. http://www.sciencedirect.com/science/article/pii/S0370269307011732.

[32] **Borexino** Collaboration, G. Bellini *et al.*, "First evidence of pep solar neutrinos by direct detection in Borexino," *Phys.Rev.Lett.* **108** (2012) 051302, arXiv:1110.3230 [hep-ex].

[33] G. Bellini *et al.*, "Observation of geo-neutrinos," *Physics Letters B* **687** no. 45, (2010) 299 – 304. http://www.sciencedirect.com/science/article/pii/S0370269310003722.

[34] **Borexino** Collaboration, P. Alvarez Sanchez *et al.*, "Measurement of CNGS muon neutrino speed with Borexino," *Phys.Lett.* **B716** (2012) 401–405, arXiv:1207.6860 [hep-ex].

[35] **SNEWS** Collaboration, C. Vigorito, "SNEWS: The supernova early warning system," *J.Phys.Conf.Ser.* **309** (2011) 012026.

[36] **Borexino** Collaboration, F. Calaprice, "Solar Neutrino Results and Future Opportunities with Borexino," *Physics Procedia: TAUP* (2013) .

[37] e. a. Bahcall, John N., "Solar neutrinos: Radiative corrections in neutrino - electron scattering experiments," *Phys.Rev.* **D51** (1995) 6146–6158, `arXiv:astro-ph/9502003 [astro-ph]`.

[38] P. Moistero, "First detection of pp neutrinos in real time in the borexino detector," *PhD Thesis, Princeton University* (2014) .

[39] J. BIRKS, "The theory and practice of scintillation counting," International Series of Monographs in Electronics and Instrumentation. Pergamon, 1964. `http://www.sciencedirect.com/science/article/pii/B9780080104720500100`.

[40] **Borexino** Collaboration, K. Otis, "Documentation on the synthetic spectra," *Internal Borexino Memo* (2014) .